ACS APPLIED MATERIALS & INTERFACES

www.acsami.org

Research Article

Temperature-Induced Conversion of 2D Vanadium-Doped $MoSe_2$ Nanosheets to 1D V_2MoO_8 Rods: Enhanced Performance in Electrochemical Antibiotic Detection in Biological and Environmental Samples

Raj Karthik, Ramaraj Sukanya,* Prajakta R. Chavan, Mahmudul Hasan, Eswaran Kamaraj, Carmel B. Breslin,* Jintae Lee, and Jae-Jin Shim*

Cite This: *ACS Appl. Mater. Interfaces* 2024, 16, 29374−29389

Read Online

ACCESS | Metrics & More | Article Recommendations | Supporting Information

ABSTRACT: In this work, new strategies were developed to prepare 1D-V_2MoO_8 (VMO) rods from 2D V-doped $MoSe_2$ nanosheets ($VMoSe_2$) with good control over morphology and crystallinity by a facile hydrothermal and calcination process. The morphological changes from 2D to 1D rods were controlled by changing the calcination temperature from 300 to 600 °C. The elimination of Se and the incorporation of O into the V−Mo structure were evaluated by TGA, p-XRD, Raman, FE-SEM, EDAX, FE-TEM, and XPS analyses. These results prove that the optimization of the physical parameters leads to changes in the crystal phase and textural properties of the prepared material. The $VMoSe_2$ and its calcined products were investigated as electrochemical sensors for the detection of the antibacterial drug nitrofurantoin (NFT). At a calcination temperature of 500 °C, the modified screen-printed carbon electrodes (SPCE) proved to be an excellent electrochemical sensor for the detection of NFT in neutral media. Under the optimized conditions, VMO-500 °C/SPCE exhibits low detection limit (LOD) (0.015 μM), wide linear ranges (0.1−31, 47−1802 μM), good sensitivity, and selectivity. The proposed sensor was successfully used for the analysis of NFT in real samples with good recovery results. Moreover, the reduction potential of NFT agreed well with the theoretical analysis using quantum chemical calculations, with the B3LYP with 6-31G(d,p) basis set predicting an E^0 value of −0.45 V. The interaction between the electrode surface and NFT via the LUMO diagram and the electrostatic potential surface is also discussed.

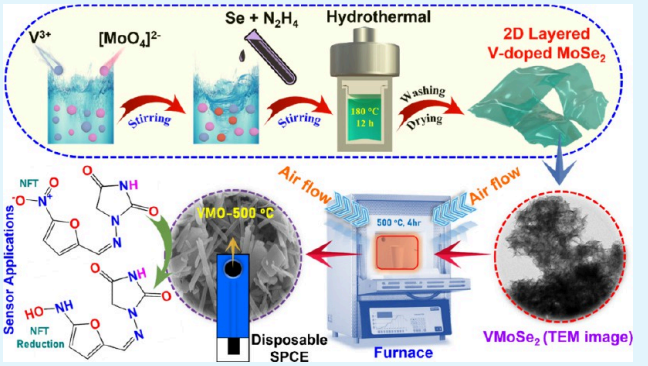

KEYWORDS: *vanadium-doped $MoSe_2$, binary metal oxide, 2D-nanosheet, 1D-nanorods, nitrofurantoin sensor*

1. INTRODUCTION

Binary metal oxides ($A_{1+x}Mo_xO_8$) have drawn much attention due to their interesting electrochemical properties that stem from polymorphism, high conductivity, and suitable redox levels of the charge carriers or different oxidation states of the metal ions.[1−3] Compounds such as $Fe_2Mo_3O_8$, $Zn_2Mo_3O_8$, and $Co_2Mo_3O_8$ have been used as electrode materials for supercapacitors, batteries, and electrochemical sensors.[2−4] Among these, molybdenum−vanadium or vanado−molybdate (V−Mo−O_x) oxides, which belong to the family of V_2O_5−MoO_3 systems and consist of various combinations such as VO_x−MoO_y,[5] $Mo_{0.88}V_{0.12}O_{2.94}$,[6] $VMoO_x$,[7] and $V_{3.6}Mo_{2.4}O_{16}$,[8] are particularly interesting in terms of electrochemical applications. The electrochemically active and conducting V and Mo metals lead to easily accessible redox couples.[7,9,10] Besides, the high redox behavior of V and the conductivity of Mo lead to a strong synergism, which increases the intrinsic activity of the overall V−MoO_x compounds.[11] Furthermore, the presence of V in $VMoO_x$ leads to a volume change and shortens the ion diffusion path, enhancing electron transport between the electrode and electrolyte interfaces. This was demonstrated by Miao et al., who introduced a layered V_2MoO_8 material by electrospinning and developed it as an electrode for Li-ion batteries due to its low molecular weight and high electronegativity.[12] The electrochemical properties of V_2MoO_8 mainly result from the structural combination of one-dimensional arrangements consisting of face-sharing octahedra, isolated VO_4, and discrete MoO_4 tetrahedra, which determines

Received: February 7, 2024
Revised: May 8, 2024
Accepted: May 13, 2024
Published: May 23, 2024

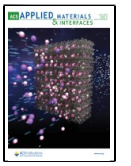

https://doi.org/10.1021/acsami.4c02022
ACS Appl. Mater. Interfaces 2024, 16, 29374−29389

its promising electrochemical properties.[12] It is believed that the presence of these discrete tetrahedra, which form the main structure, is an essential component to stabilize the surface during the electrochemical process.[12,13]

However, combining and fabricating molybdate clusters with different nanostructures using simple techniques is still a challenge. The synthesis of metal molybdates with various morphologies such as nanoflakes,[14] nanosheets,[15] nanowires,[16] nanoplates,[17] and some microstructures[18] has been reported previously and used for electrochemical applications. However, the synthesis of the V_2MoO_8 phase is quite complicated and leads to structural disorder (Wadsley defects) and size variations that can lead to low ionic interactions. Several methods have been reported in articles for synthesizing V_2MoO_8, including solid-state methods,[19] electrospinning,[12] and ball milling.[13] However, these approaches and associated studies often necessitate multiple steps to attain the desired phase, along with high calcination temperatures. The synthesis of molybdates based on metal−organic frameworks (MOFs) has been proposed to overcome this problem. For example, Li et al. reported the fabrication of $CoMoO_4$ using a self-supporting cobalt-based MOF template by a microwave-assisted method and then obtained arrays of $CoMoO_4$ nanosheets for the fabrication of binder-free electrodes for supercapacitors.[20] Unfortunately, the "$MMoO_x$" structures derived from MOFs have no clear geometric structure and have low conductivity, which makes them unsatisfactory for electrochemical applications.[21] Therefore, in this article, we have attempted to prepare 1D-V_2MoO_8 rods (VMO) from 2D vanadium-doped molybdenum diselenide nanosheets ($VMoSe_2$ NSs) by a simple hydrothermal approach followed by a calcination process and have successfully used them as electrode materials for the electrochemical sensing of the antibiotic drug nitrofurantoin (NFT).

As an antibiotic, NFT (5-membered ring) is widely used to treat various Gram-positive/-negative bacteria (*Staphylococcus saprophyticus*, *Enterococcus faecalis*, *Streptococcus agalactiae*, *Escherichia coli*, and *Klebsiella* species) and protozoan infections.[22,23] It is also commonly prescribed for the treatment of pulmonary toxicity, bladder cancer, hepatitis, and hemolytic anemia.[24,25] At the same time, excessive use of NFT affects humans and causes various health problems such as nausea, headache, abdominal pain, neuropathy, drowsiness, diarrhea, and dizziness.[26,27] Therefore, close monitoring of the levels of NFT in water and biological samples is essential. Electrochemical sensing offers unique advantages compared to other techniques, such as high selectivity, portability, and good sensitivity.[27] In our previous study, Vinoth Kumar and Karthik et al. presented the synthesis of $Nd_2Mo_3O_9$ for the electrochemical detection of NFT and achieved a good detection limit (16 nM) and sensitivity.[25] In addition, lanthanum molybdate (LMNS) modified electrodes prepared by Balamurugan et al. showed good electrocatalytic activity for the detection of NFT and achieved a detection limit of 0.072 μM.[23] To enhance the electrochemical detection of NFT, we propose the introduction of a novel metal molybdate, comprised of VMO rods derived from 2D-$VMoSe_2$ nanosheets (NSs). Notably, these rods have not been previously explored for sensing applications. Given the challenges associated with VMO synthesis, we present a straightforward synthesis approach for the first time, along with an evaluation of its electrochemical performance as an NFT sensor.

In this study, we outline a successful method for preparing VMO rods through a straightforward synthesis process utilizing 2D-$VMoSe_2$ as the precursor. Initially, $VMoSe_2$ NSs are synthesized via a simple hydrothermal method. Upon confirmation of the structure, the fabricated $VMoSe_2$ NSs undergo a thermal treatment at elevated temperatures (300, 400, 500, and 600 °C) to eliminate Se atoms from the lattice via evaporation. This process leads to the formation of various crystalline phases of V_xMoO_x and the morphological transformation from NSs to rods. Our work elucidates the transition of 2D chalcogenide nanosheets in the amorphous phase to 1D rods. The resulting 1D-VMO rods, synthesized at different temperatures, are employed as electrode materials for the electrochemical detection of NFT utilizing disposable screen-printed carbon electrodes (SPCE).

2. EXPERIMENTAL SECTION

The Supporting Information (see Sections S2.1−S2.4) provides comprehensive details regarding the chemicals/reagents used, characterization techniques employed, electrode fabrication procedures, electrochemical measurement methods for NFT detection, and preparation of real samples.

2.1. Synthesis of 2D-$VMoSe_2$ NSs and 1D-VMO Rods. In a typical synthesis, 0.02 M $Na_2MoO_4{\cdot}2H_2O$ (0.24 g) and 0.02 M VCl_3 (0.15 g) were mixed in 30 mL double distilled water (DD) and stirred magnetically for up to 20 min. About 0.15 g (0.04 M) of Se powder was added to this solution and stirred again for 30 min. Then 10 mL of hydrazine monohydrate solution was slowly dropped into the above solution, which turned into a black-colored solution. The final solution was stirred for 30 min to obtain a homogeneous mixture. Finally, the black-colored solution was transferred to a 100 mL autoclave equipped with Teflon and kept in a hot air oven at 180 °C for 12 h. After hydrothermal treatment, the mixture was allowed to cool to room temperature. Then the obtained precipitate was collected and washed several times with water/ethanol and finally dried overnight at 45 °C.

To prepare the 1D-VMO rods, the collected black $VMoSe_2$ powder was calcined in air at different temperatures (300, 400, 500, and 600 °C, ramp/cooling rate 2 h) for 4 h. Temperature optimization was used to remove Se from the lattice by an evaporation process to obtain a final product with 1D-VMO rods. This overall process is summarized in Scheme 1.

2.2. Density Functional Theory (DFT) Calculation. Quantum chemical calculations were performed with the package Gaussian 09. DFT calculations were performed for the ground state structure using the unrestricted B3LYP functional (Becke's three-parameter hybrid exchange functional with Lee−Yang−Parr correlation) with the 6-31G(d,p) basis set. For the solvent energies (water), the polarizable continuum model with the integral equation formalism (IEFPCM) was used. The free energy values were taken from the Gaussian output files as the "sum of electronic and thermal energies" in the frequency analyses.

The methodology described in the literature was used to evaluate the standard reduction potential, as described by eq 1.[49,50]

$$E^0 = \frac{\Delta G^{\mathrm{Red}}_{(\mathrm{solv})}}{nF} \tag{1}$$

where n is the number of electrons involved in the reduction reaction and F is Faraday's constant. The reduction potential $\Delta G^{\mathrm{Red}}_{(\mathrm{solv})}$ was determined using the Born−Haber thermodynamic cycle, as shown in Scheme 2. It is based on the change in the Gibbs free energy of the gas phase and the free energy of solvation of the oxidized state and the reduced state and leads to eq 2:

$$\Delta G^{\mathrm{Red}}_{(\mathrm{solv})} = \Delta G^{\mathrm{Red}}_{(\mathrm{g})} + \Delta G^{\mathrm{Red}}_{(\mathrm{s})} - \Delta G^{\mathrm{Ox}}_{(\mathrm{s})} \tag{2}$$

The computation of the change in free energy then has the form $\Delta G^{\mathrm{Red}}_{(\mathrm{g})} = \Delta U^{\mathrm{Red}}_{(\mathrm{g})} + PV - T\Delta S^{\mathrm{Red}}_{(\mathrm{g})}$, where the corrections for the

https://doi.org/10.1021/acsami.4c02022
ACS Appl. Mater. Interfaces 2024, 16, 29374−29389

Scheme 1. Overall Synthesis Procedure for the Preparation of 1D-VMO from the 2D-VMoSe$_2$ NSs

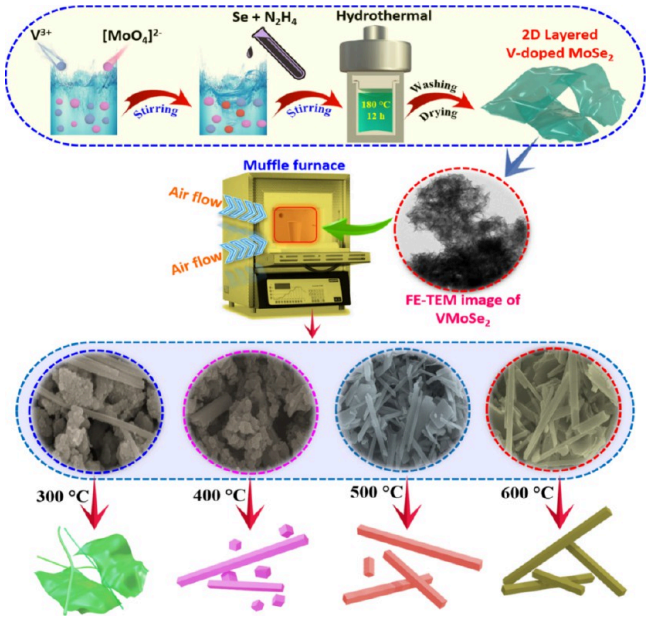

Scheme 2. Representation of the Born−Haber Thermodynamics Cycle

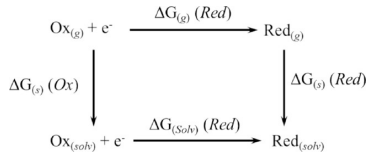

vibration, rotation, and translation contributions to entropy were determined on the basis of the vibration frequency calculations.

3. RESULTS AND DISCUSSION

3.1. Structural and Morphological Evaluation from 2D to 1D. The conversion of 2D-VMoSe$_2$ NSs into 1D-VMO was achieved in two steps: (i) initial formation of the VMoSe$_2$ layered morphology by the hydrothermal method and (ii) a calcination treatment to obtain VMO. The hydrothermal formation of VMoSe$_2$ in the presence of N_2H_4 at a temperature of 180 °C for 12 h occurs in two reaction steps (i.e., nucleation and crystal growth). During nucleation, the symmetry and phase structure determine the morphology or texture, while crystal growth depends on the temperature. Through optimized heat treatment and the use of solution reactants, the formation of VMoSe$_2$ was achieved by the self-assembly of the core centers. VMoSe$_2$ is primarily synthesized by a hydrothermal approach in the presence of N_2H_4 as a reducing agent and at a temperature of 180 °C for 12 h. The reaction first occurs between precursors such as sodium molybdate monohydrate, which serves as Mo ions, and vanadium chloride, which provides V ions. The V/Mo ions then react during the hydrothermal process to form the unstable vanadium molybdenum-based product. At the same time, the Se atoms are reduced by reaction with N_2H_4 at high temperature (180 °C) to Se^{2-} ions, which are then bound to the vanadium molybdenum-based product. Over a long period of time (12 h), the Se^{2-} ions react with vanadium−molybdenum to form the final VMoSe$_2$. After completion of the reaction, the particles exhibit a multilayered, sheet-like morphology. The obtained layered VMoSe$_2$ was used to synthesize the VMO rods by calcination at different temperatures. The schematic diagram of the stepwise synthetic process is shown in Scheme 1. A known amount of the prepared VMoSe$_2$ was taken for the calcination process, which was carried out in the air by switching the temperature from 300 to 600 °C. Due to the lower melting point, the Se in the VMoSe$_2$ lattice was removed by evaporation, and this supported the formation of the different phases of V_xMoO_x. This thermal process leads to the formation of mixed phases of V−Mo-based oxides. The compound has mixed phases and a different morphology depending on the temperature. At 500 and 600 °C, the mixed phases transform completely into a single VMO phase with minor impurities (MoO_3 according to the XRD results), changing the morphology from nanosheets to nanoparticles and finally to rods. The obtained powders were collected for analysis to confirm their phase and morphology changes.

First, the phase transformations of VMoSe$_2$ into VMO were investigated by p-XRD analysis. The corresponding XRD patterns for all samples are shown in Figure 1(A). The XRD pattern for VMoSe$_2$ (Figure 1(A)) shows the presence of broad peaks at angles of 14.04°, 32.0°, 34.64°, 42.22°, and 56.42°, corresponding to planes (002), (100), (102), (006), and (110), respectively. They are in perfect agreement with the amorphous phase of multilayered molybdenum diselenides ($MoSe_2$), which are hexagonally symmetric (JCPDS No. 00−029−0914).[28,29] The angles of the (002), (100), (102), (006), and (110) planes of VMoSe$_2$, obtained in this study, show slight positive shifts compared to pristine $MoSe_2$. This suggests the complete integration/doping of V atoms into the $MoSe_2$ lattice, with no other impurities present. Additionally, Figure 1(A) in the XRD pattern illustrates the phase transitions of VMoSe$_2$ to VMO across temperature variations from 300 to 600 °C.

As can be seen in Figure 1(A), the sample at 300 °C shows the formation of a peak at 21.9° with a slight shift of the other peaks at 33.14° and 54.03° toward the positive side, indicating the formation of a smaller amount of oxygen (formation of VMoO) along with the presence of the $MoSe_2$ phase. As the temperature increases, some characteristic diffraction peaks of VMO appear, indicating that the phase transition from the amorphous to the crystalline state begins at 400 °C.[12] Even at 400 °C, the diffraction peaks show a small peak of MoO_3 in addition to VMO. However, the remaining Se ions have been completely removed from the lattice due to their instability at higher temperatures (according to TGA analysis). At 500 °C, the crystallinity of the XRD peaks increases, with the intensity of the peaks increasing, proving that the phase transition from the amorphous to the crystalline state is complete, which is obviously to be expected at higher temperatures. Moreover, the splitting of the peaks in the XRD patterns during the transition from 400 to 500 °C clearly proves the occurrence of a phase transition. Apart from this, the diffraction peaks' crystallinity increases, and the VMO is successfully formed. Besides, the as-prepared metal oxides (400−600 °C) revealed the presence of two very intense planes: the (001) plane at 21.55° and the (110) plane at 24.92°, with corresponding *d*-spacing values of 0.412 and 0.357 nm, respectively. The determination of *d*-spacing values and average crystallite size was achieved using eqs 3 and 4, respectively, yielding the results summarized in Table S2.

https://doi.org/10.1021/acsami.4c02022
ACS Appl. Mater. Interfaces 2024, 16, 29374−29389

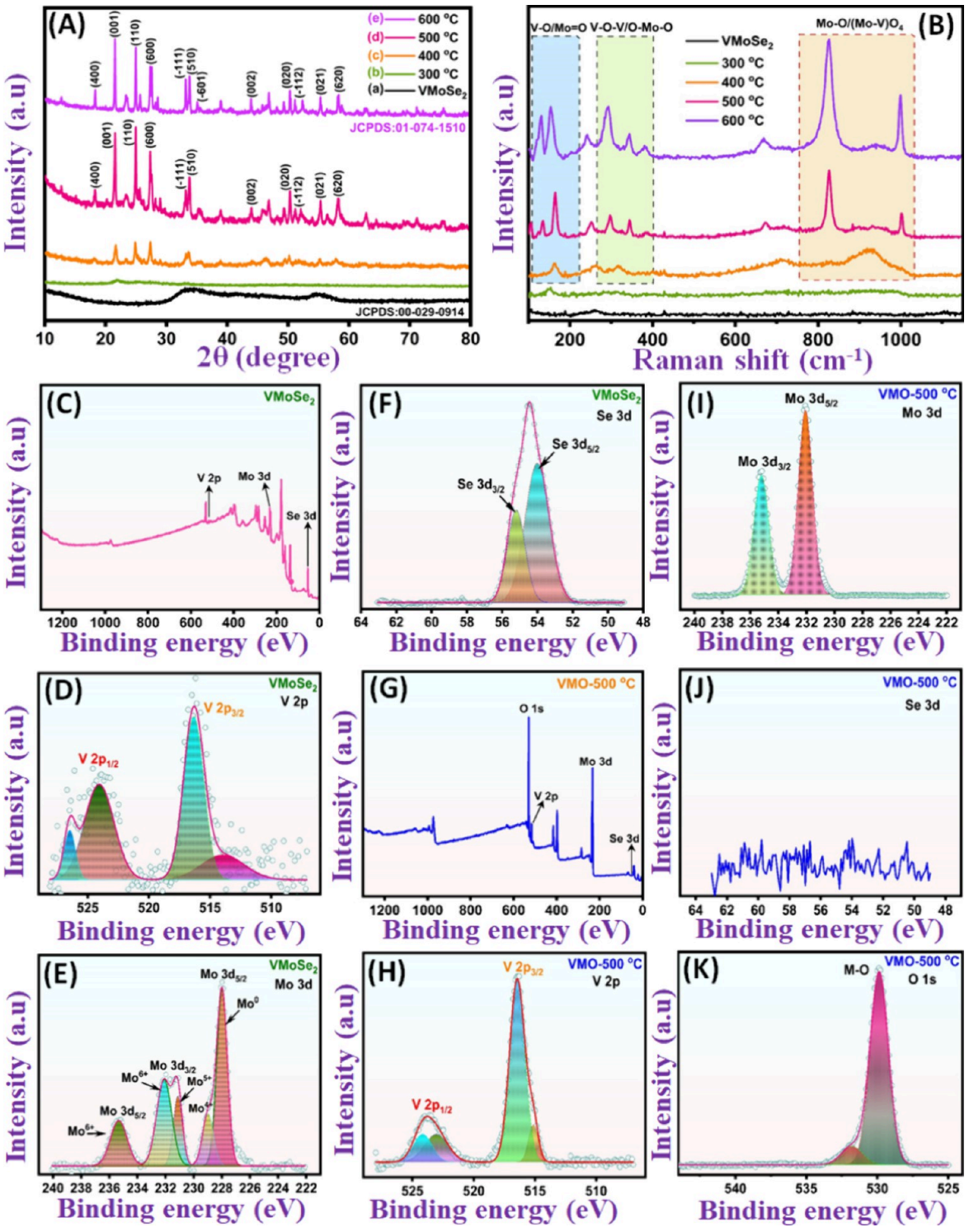

Figure 1. (A) p-XRD and (B) Raman spectra of $VMoSe_2$ at different calcination temperatures. (C, G) Overall survey spectra of $VMoSe_2$ and VMO-500 °C. High-resolution XPS spectra of (D) V 2p, (E) Mo 3d, (F) Se 3d in $VMoSe_2$, and (H) V 2p, (I) Mo 3d, (J) Se 3d, and (K) O 1s in VMO-500 °C.

$$d = n\lambda/2 \sin \theta \quad (3)$$

$$D = K\lambda/\beta \cos \theta \quad (4)$$

The data presented in Table S2 indicate that the 2θ value and d-spacing value of the as-prepared VMO at different temperatures closely align with the theoretical values. However, the average crystallite size of the materials exhibits an increase proportional to the calcination temperature. This phenomenon can be attributed to the growth of crystallites as the calcination temperature rises, which leads to the elimination of irregularities, edges, and defects within the crystal structure.[51] However, a trace of MoO_3 is also present in the same sample, the intensity of which is comparatively negligible. The XRD standard patterns for V_2MoO_8 (red line) and MoO_3 (blue line) (JCPDS No. 01−076−1003) are shown in Figure S1. Further increasing the temperature to 600 °C shows a similar trend as

https://doi.org/10.1021/acsami.4c02022
ACS Appl. Mater. Interfaces 2024, 16, 29374−29389

at 500 °C, but the intensity of MoO_3 is comparatively higher. At a temperature higher than 600 °C, the intensity of MoO_3 also increases in addition to the VMO phase. Therefore, the main goal of this work is to synthesize the VMO phase without other impurities, so we do not focus on temperatures above 600 °C.

The XRD patterns of VMO obtained at 500 °C (VMO-500 °C) show prominent peaks with high intensity at angles of 18.24°, 21.58°, 25.01°, 27.63°, 33.21°, 33.84°, 35.07°, 43.88°, 50.34°, 51.14°, 55.36°, and 58.22°, corresponding to *hkl* planes (400), (001), (110), (600), (−111), (510), (−601), (002), (020), (−112), (021), and (620), respectively. The strong diffraction peaks agree well with the previously published articles[12,30] and correlate with the standard card value (JCPDS-ICDD 01−074−1510). From this XRD analysis, the VMO formed at 500 °C has a monoclinic unit cell with dimensions a = 19.39 Å, b = 3.62 Å, and c = 4.11 Å and belongs to the space group $C2$. The additional diffractions were defined as continuous streaks, which could indicate the existence of 1D structures. Moreover, the peak at 24.92°, corresponding to the plane of (110), shows a higher intensity and is dominant over the other peaks. This phenomenon is probably due to the preferential growth of the low-index peak (110) during the thermal treatment, in which the main starting material, $VMoSe_2$, oriented in the same crystallographic plane is transformed into the final product (VMO), indicating the maintenance of the phase relationship with the precursor during the transformation of the layered into bulk rods. It was evident that the disorder in the V−Mo compounds mainly results from their distribution around the tetrahedral sites, affecting the cationic sites (vacancies) and the discrete tetrahedra.[12] Finally, this type of tetrahedral site contains the bulk structure in the form of 1D, which is an essential component for the efficient diffusion of ions/analytes during the electrochemical process. Finally, the results of the XRD analysis confirmed that the temperature change affects the crystallographic phase. Moreover, the Rietveld refinement was carried out using the Fullprof Suite software, considering two phases (Figure S2). One is VMO, which falls into space group C 1 2/m 1 with a monoclinic symmetric unit cell. The other is MoO_3, which falls into the *Pbnm* space group. In the refined XRD pattern, two Bragg positions, the upper one for VMO and the lower one for MoO_3, indicate the presence of two phases in the prepared materials. Moreover, the cell volume of VMO is 290.04 Å^3[52] and of MoO_3 is 203.041 Å3,[53] while the cell volume of our material is 289.57 Å^3 (Table S1). A small decrease in the volume of the material compared to VMO confirms the presence of a small amount of MoO_3.

To ensure Se elimination, TGA measurements were performed for the fabricated $VMoSe_2$ under N_2 flow in the temperature range of 25−900 °C to calculate the Se loss in the materials. As shown in Figure S3, a slight weight loss was observed for the pure phase of $VMoSe_2$ between 200 and 318 °C, which is in good agreement with the previously reported $MoSe_2$-based articles.[31] This weight decrease can be attributed to the oxidation of $VMoSe_2$. When the temperature is further increased (from 318 °C or up to 500 °C), volatilization takes place, leading to a final residue of VMO, with SeO_2 escaping simultaneously.[32] This thermal analysis of $VMoSe_2$ is consistent with the elimination of Se at temperatures above 200 °C (melting point of Se is 217 °C) and the formation of the V−Mo-based oxides. These TGA results are in good agreement with the XRD results and indicate a drastic phase change during the calcination process. To further confirm the removal of Se from $VMoSe_2$, the photocopies before and after calcination are shown in Figure S4, which clearly show that the prepared powder was black before calcination, and after calcination the black color changed to a light gray color. This is a clear indication that the NSs were successfully converted into rods by increasing the temperature.

Compared to p-XRD, Raman analysis provides clear indications of the structural information on the proposed materials, such as $VMoSe_2$ and VMO. As shown in Figure 1(B), the Raman peaks of $VMoSe_2$ reveal the presence of prominent peaks at low values of 257.9 and 427.7 cm^{-1}, representing the out-of-plane A_{1g} and in-plane E^1_{2g} vibrational modes in the hexagonal phase of $MoSe_2$.[33] Compared to the original $MoSe_2$, a slight shift in the vibrational modes is observed, which might be related to the doping of V on the $MoSe_2$ basal surface. In addition, the intensity of the E^1_{2g} mode is lower than the A_{1g} mode, indicating the presence of rich edge sites in the fabricated $VMoSe_2$ nanosheets.[33,34] After the calcination process, the Raman spectrum at 300 °C shows the vibrational modes of both $VMoSe_2$ and VMO materials. However, with the temperature increase to 400 °C, an additional vibrational mode was observed at 163.3 and 316.8 cm^{-1}, which is related to the VO_4 tetrahedra or the edge-sharing distorted MoO_6 of the V−O or O−Mo−O bond.[35,36] When the temperature was increased from 400 to 500 °C or 600 °C, the Raman active bonds of the Mo−Se changed completely to Mo−O, indicating the successful formation of V−Mo-based oxides. When the temperature was increased from 300 to 400 °C, new peaks appeared at 260.48 and 713 cm^{-1}, corresponding to the M═O bending vibration and the vibration of the Mo−O_3 bridge bond of MoO_3.[54,55] However, the peaks shifted to lower wavenumbers when the calcination temperature was increased, which could be due to the higher crystallinity of VMO. In comparison, the sample at 500 °C exhibits several active Raman peaks at 134.1 cm^{-1}, 163.3 cm^{-1}, 251.4 cm^{-1}, and 296.5 cm^{-1}, which can be assigned to the bending and stretching vibration modes of V−O or Mo═O bonds. The peaks at 134.1 cm^{-1}, 163.3 cm^{-1}, and 251.4 cm^{-1} can be assigned to the edge-sharing distorted MoO_6 (O−Mo−O) octahedra.[36] The peaks at 296.5 and 343.3 cm^{-1} can be assigned to the symmetric stretching vibrations of the V−O−V (VO_4) and O−Mo−O bonds, respectively.[37,38] The peak at 673 cm^{-1} belongs to the asymmetric V−O stretching vibration mode (B_g symmetry). The asymmetric stretching vibrations of Mo−O (MoO_4) at 826.6 cm^{-1} and a symmetric stretching of M═O−V (Mo/V)O_4 tetrahedra at 1002.4 cm^{-1} were also observed.[36] From these spectra, the V−Mo−O bonds are smaller than the obtained Mo−O bond length but longer than the V−O bond length, indicating that there are more valence states for Mo than for V in the fabricated VMO structure, which may lead to better electrochemical performance toward sensing.[39] A similar trend was also observed for the samples thermally treated at 600 °C. The above Raman analyses prove that the temperature-controlled reaction is essential for the preparation of VMO materials. Moreover, the Raman measurements agree with the XRD analysis, which means that the phase transition from Mo−Se to Mo−O bonds is indeed possible during this temperature-controlled reaction.

After confirming the phase changes during the temperature-induced reactions of $VMoSe_2$ to VMO (VMO-500 °C), we investigated these material surface reactions and the chemical composition by XPS analysis. The survey spectra for $VMoSe_2$

https://doi.org/10.1021/acsami.4c02022
ACS Appl. Mater. Interfaces 2024, 16, 29374−29389

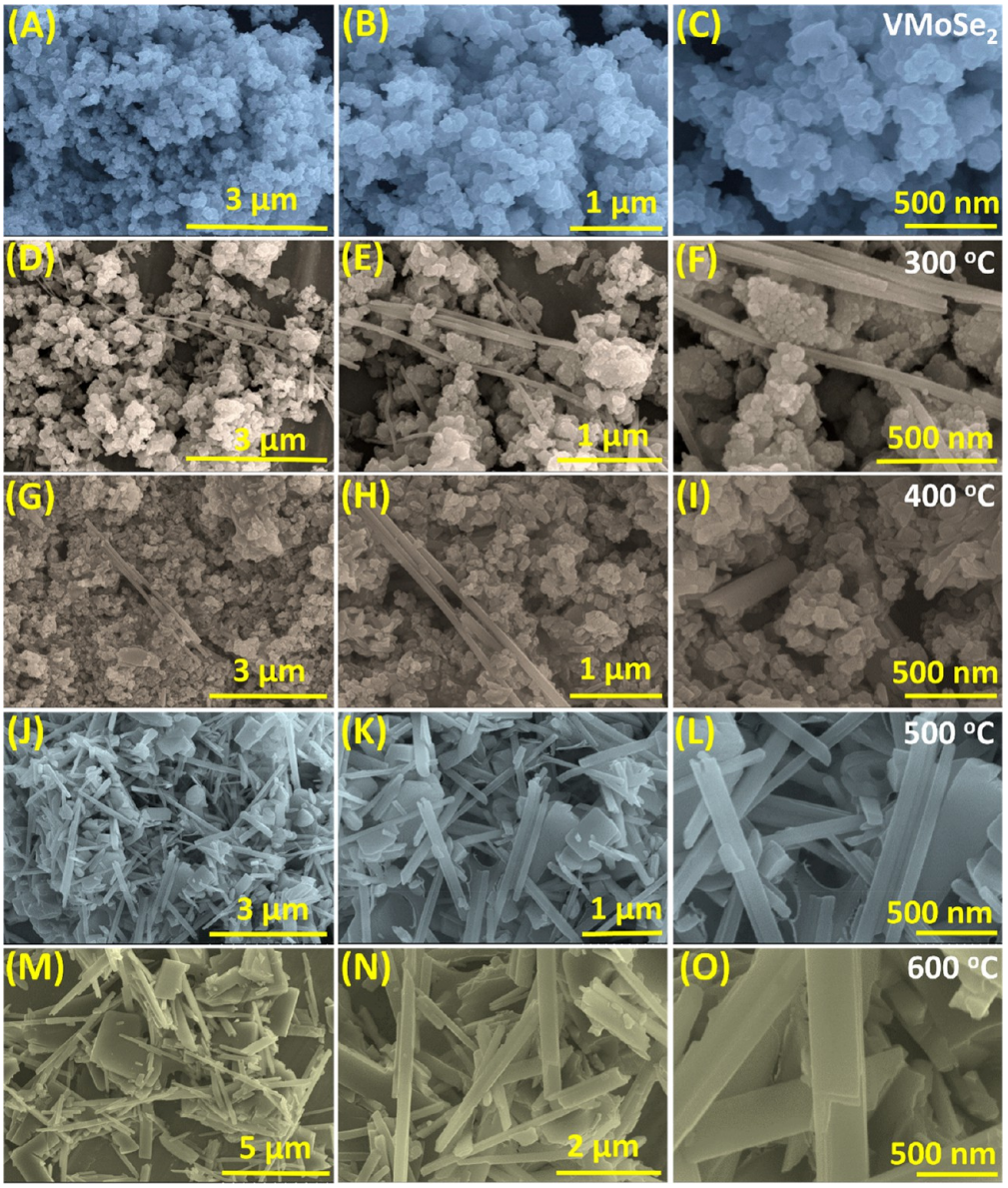

Figure 2. FE-SEM images with different magnifications of (A–C) $VMoSe_2$, (D–F) VMO-300 °C, (G–I) VMO-400 °C, (J–L) VMO-500 °C, and (M–O) VMO-600 °C.

are shown in Figure 1(C) and confirm the presence of elements such as V, Mo, and Se, respectively. Calcination of $VMoSe_2$ to VMO after treatment at 500 °C yielded an overview spectrum indicating the presence of elements such as V, Mo, and O with slight variations in binding energies and oxidation states (see Figure 1(G)). The individual core spectra of V in $VMoSe_2$ (Figure 1(D)) show four XPS peak fittings at binding energies of 513.9, 516.2, 524.06, and 526.7 eV, corresponding to subshells V $2p_{3/2}$ and V $2p_{1/2}$, respectively. In addition, this core spectrum shows mixed oxidation states for vanadium during the synthesis process, including V^{4+} and V^{5+}. After calcination to VMO, the V core spectra (Figure 1(H)) show similar deconvoluted peaks with a slight shift in binding energy values of 515.1, 516.4, 523.01, and 524.16 eV corresponding to the same oxidation states.[40,41] However, the variation in intensity and the shift in binding energy suggest characteristic changes in the chemical and physical environment of the species. In the case of the Mo core spectra (Figure 1(E)), there are several characteristic peaks deconvoluted to binding energies of 229.1, 231.1, 232.0, and 235.3 eV, which are mainly assigned to the Mo $3d_{5/2}$ and Mo $3d_{3/2}$ subshells in the $VMoSe_2$.[34,42] Moreover, a strong peak at 227.9 eV corresponds to the metallic phase of Mo (Mo^0).[43] The resolved Mo 3d peaks show the presence of strongly mixed valence states of Mo^{6+}, Mo^{5+}, and Mo^{4+}, respectively. However, in VMO (Figure 1(I)), the Mo 3d exhibits only two main peaks at binding energies of 232.2 and 235.0 eV, which can be attributed to the Mo^{6+} valence states in the V–Mo oxide phase. This reduction in peaks is comparable to a phase change during the conversion of $VMoSe_2$ to VMO. Compared to Mo, V shows similar fitting peaks for its deconvoluted XPS spectra, suggesting that the electronic cloud around the V atom is larger than around the Mo atom in the fabricated VMO lattice. The scan spectrum of Se 3d is also shown in Figure 1(F) and shows two peaks at the binding energies of 54.0 and 55.1 eV, belonging to the subshells Se $3d_{5/2}$ and Se $3d_{3/2}$, respectively, which belong to the Mo–Se bond in $VMoSe_2$.[41] After the calcination process, the absence of Se atoms in VMO

https://doi.org/10.1021/acsami.4c02022
ACS Appl. Mater. Interfaces 2024, 16, 29374–29389

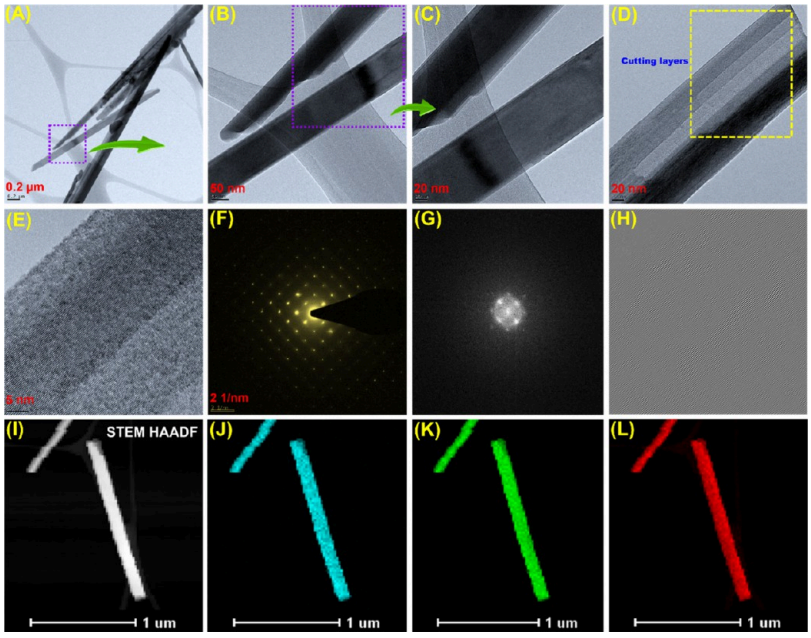

Figure 3. (A–E) FE-TEM images with different magnifications of VMO-500 °C, (F) SAED pattern, (G) FFT pattern, (H) inverse FFT pattern (IFFT), (I) STEM-HADDF resolved dark field image, and (J–L) area scan mapping images of VMO-500 °C (V (J), Mo (K), and O (L)).

was assessed by XPS scan spectra (Figure 1(J)), and no peaks for Se were generated, proving the successful removal of Se after calcination at the higher temperature. The removal of Se was also evident when analyzing the O atoms, which was confirmed by the scan spectra of O 1s shown in Figure 1(K). The core spectra of O 1s show the presence of two peaks at the binding energies of 529.8 and 531.7 eV associated with the metal–oxygen bond (V–Mo–O), and the "O" species appear at the subsurface of the oxides.[5,44] From the above O 1s spectrum, the Se was successfully removed, and a VMO phase was obtained by a simple calcination process.

After analyzing the phase transition, the change in morphology from 2D NSs to 1D rods was further investigated using FE-SEM and FE-TEM. The corresponding FE-SEM images are shown in Figure 2(A–O). Figure 2(A–C) indicates the formation of multilayer $VMoSe_2$ NSs, whose surface has a uniform size and shape. The surface of the layers exhibits a 2D-like morphology, confirmed by the FE-TEM analysis. The stepwise formation of $VMoSe_2$ NSs into VMO rods upon heat treatment from 300 to 600 °C can be clearly seen in Figure 2(D–O). From Figure 2(D–F), there is a mixed morphology of VMo–O and VMo–Se when the temperature reaches 300 °C. The layers are aggregated into some rods of V–MoO_x together with layered particles of $VMoSe_2$. This type of mixed morphology of the samples indicates the incomplete removal of Se even when the temperature is above the melting point. When the temperature increases to 400 °C, the layered materials are combined and formed into smaller VMO rods with larger thicknesses and smaller sizes (Figure 2(G–I)).

More specifically, the bulk layers of the mixed phase were more aggregated to produce rod-like VMO. When the temperature was further increased to 500 and 600 °C (Figure 2(J–O)), the small rods aggregated more and grew into large rods with 1D. In addition, the surface of each rod is smoother and longer. No significant change in morphology was observed, and the 1D rod was maintained even when the temperature was increased from 500 to 600 °C. In addition to the rods, a small amount of flake-like morphology was also observed, possibly due to the MoO_3 at 500 and 600 °C, which is in good agreement with the p-XRD results. Moreover, these VMO rods belong to the 1D and have a larger surface area and more accessible active sites which can promote electron transfer and improve the electrochemical performance. Finally, the FE-SEM analysis revealed that the rod's morphology and size changed when the phase changes occurred during the temperature fluctuations from 500 to 600 °C. These results provide clear evidence that the stepwise preparation of VMO from $VMoSe_2$ leads to structural and phase changes. In addition to FE-SEM, elemental analysis (EDAX) was performed to confirm the presence of elements before and after the synthesis of the final VMO rods and to demonstrate the successful removal of Se. Figure S5(A,B) shows the corresponding EDAX spectrum for the two samples, $VMoSe_2$ and VMO-500 °C. Based on this analysis, we were able to confirm the presence and percentage ratio (at.%) of all elements in the two samples, $VMoSe_2$ (V (1.7), Mo (32.6), and Se (65.5)) and VMO-500 °C (V (11.8), Mo (16.2), O (71.8), and Se (0.0)). The results of the element mapping and EDAX spectra of $VMoSe_2$, VMO-300 °C, VMO-400 °C, and VMO-600 °C are shown in Figures S6–S9. It can be clearly seen that when the temperature was increased from 300 to 600 °C the Se evaporated, and the oxygen was successfully incorporated into the V–Mo structure.

In addition, the average size distribution of the VMO rods was analyzed using dynamic light scattering (DLS), and the obtained results are provided in the Supporting Information (see Section S2.5, Figure S10). From the analysis, the average rod size distribution of the VMO-500 °C sample is ~739.6 nm with a polydispersity index (PDI) of 0.338. Further explanations of the DLS results for VMO-500 °C can be found in the Supporting Information.

To clarify the morphological change from $VMoSe_2$ NSs to VMO rods, FE-TEM analysis was performed. As shown in Figure S11, the hydrothermally synthesized $VMoSe_2$ exhibited multiple thin layers with a nanosheet, as expected. The NSs have more active edge sites (defective sites), which can be converted into catalytic sites after the synthesis of VMo-based

https://doi.org/10.1021/acsami.4c02022
ACS Appl. Mater. Interfaces 2024, 16, 29374–29389

oxides. The formation of VMO rods was confirmed by analyzing the sample heated at 500 °C. Figure 3(A–D) shows the corresponding FE-TEM images for VMO formed at a temperature of 500 °C. The FE-TEM images show the formation of several transparent 1D rod-like structures of VMO. These fine rods are longer and have a smoother surface, which is consistent with the analysis of FE-SEM. From the high-resolution images in Figure 3(C), it can be deduced that the average diameter of the rods is 107 nm and has an average length of 1–2 μm (Figure 3(A)). As mentioned earlier, longer rods have a higher proportion of active sites, which contributes to more electrochemical reactions taking place during the detection of analytes. In addition, the formation of larger rods mainly arises from the combination of a larger number of thin rods, which can be seen from the formation of cut layers in Figure 3(D) (marked by the yellow dotted line). The lattice fringes of VMO rods with interlayer spacings of 0.413 and 0.374 nm corresponding to the diffraction pattern values of (001) and (110) for the monoclinic phase are shown in Figure 3(E). The formation of the crystalline phase of VMO was confirmed by the selected area electron diffraction (SAED) pattern, as shown in Figure 3(F). This indicates that the obtained product is crystalline and has a more ordered pattern, representing extreme crystallinity after the calcination process. Figure 3(G) shows the Fast Fourier Transform electron diffraction (FFT) pattern of the fabricated VMO-500 °C rods. From the FFT pattern, the patterns are arranged in ordered dotted patches, like the SAED pattern shown in Figure 3(F), which is similar to the patches of single crystal materials. This obtained FFT pattern shows the excellent crystallinity of the fabricated VMO rods after the calcination process at 500 °C. The inverse FFT image (IFFT) for VMO-500 °C is also shown in Figure 3(H). It is generated from the single crystal region and portrays the regular arrangement of some interference lattice fringes, similar to Figure 3(E). Using the line profile of the IFFT pattern (Figure S12), we calculated the *d*-spacing value of 0.374 nm and found that this value is consistent with the XRD plane value (110) for the crystalline phase of VMO. High-angle annular dark field images (STEM-HADDF) were used to analyze the VMO sample in more detail. Figure 3(I) shows the corresponding STEM-HADDF resolved dark field image of long and thin rods of VMO. The area scan mapping image of the VMO rods again proves the presence of elements such as V, Mo, and O in the prepared sample (Figure 3(J–L)). All these FE-TEM analysis results are in good agreement with the FE-SEM and p-XRD results. It is confirmed that both phase and morphological changes are possible during the variation of thermal conditions.

The formation of NSs into rods is quite complex. However, their formation is clearly connected with the removal of the Se, as seen at the higher temperatures of 500 and 600 °C. As the Se is removed, the $VMoSe_2$ is decomposed into a Mo and V solid solution, while the presence of O_2 in the atmosphere provides a source of O atoms. Consequently, the nucleation of the VMO begins as NPs with the growth of the VMO proceeding with the oriented attachment of these preformed NPs. This fusion of correctly aligned NPs will lead to a more favorable lattice-free energy. The formation of the rods indicates a variation in the surface energies of the crystallographic planes, which in turn favors the growth of the long VMO rods in one direction. Smoothing of the rods is also evident, and this may occur through conventional mechanisms of dissolution and growth, such as Ostwald ripening.[56]

3.2. Electrochemical Characterization. Before applying the detection techniques, the most important parameter for deriving the electrochemical kinetics of surface-modified and unmodified electrodes was first evaluated by electrochemical impedance spectroscopy (EIS). The EIS analysis was performed in the presence of a redox probe of 0.005 M $[Fe(CN)_6]^{3-/4-}$/0.1 M KCl solution with a frequency range of 0.1 Hz to 100 kHz, and the resulting Nyquist diagram is shown in Figure S13(A). Based on this EIS analysis, the Randle circuit model was used to fit the equivalent circuit, which includes various elements such as the charge transfer resistance (R_{ct}), Warburg impedance (W), and resistance of the electrolyte solution (R_s). The calculated values such as R_s, R_{ct}, and the Warburg coefficient (σ) are listed in Table S3. From this Nyquist diagram and Table S3, the R_{ct} value could be calculated for all electrodes from the semicircle range in the higher frequency range. The values are calculated for all electrodes such as the bare SPCE (245.1 Ω), $VMoSe_2$/SPCE (266.8 Ω), and VMO-500 °C/SPCE (1608 Ω). The bare SPCE and $VMoSe_2$ exhibit much lower R_{ct} and interfacial layer resistance, which increases the electron transfer rate. Compared to the bare SPCE and $VMoSe_2$, the VMO-500 °C/SPCE shows a much larger semicircular region due to the large electrostatic repulsive force between the negatively charged $[Fe(CN)_6]^{3-/4-}$ redox probe and the calcined V–Mo oxides.[44] Following the EIS measurement, the peak-to-peak separation (ΔE_p) and the electrochemical surface area of all prepared electrodes were recorded using cyclic voltammograms (CVs) in the presence of 0.005 M $[Fe(CN)_6]^{3-/4-}$/0.1 M KCl as a redox probe at a scan rate of 50 mV s^{-1}; these are shown in Figure S13(B). Well-defined redox peaks are observed for all electrodes in the $[Fe(CN)_6]^{3-/4-}$ probe system, and the VMO-500 °C/SPCE shows redox curves with a slightly higher shift of the positive and negative potential peaks compared to $VMoSe_2$/SPCE and bare SPCE, indicating a sluggish response at the interface between the electrode and the redox probe system due to repulsion effects. There is clear evidence of electrostatic repulsion between the calcined oxide and the negatively charged redox probe. The lowest ΔE_p value of 0.17 V was measured with the bare SPCE. The ΔE_p values were observed at 0.18 V for $VMoSe_2$/SPCE and 0.33 V for VMO-500 °C/SPCE.

In addition, the electrochemical surface area was estimated for all the electrodes by performing CVs at different sweep rates (20–200 mV/s) in the presence of 0.005 M $[Fe(CN)_6]^{3-/4-}$ with 0.1 M KCl as the electrolyte. A significant increase in peak current with increasing sweep rate (20–200 mV/s) was observed for all electrodes (Figures S14–S19). This increase in peak current is correlated with the square root of the sweep rate and plotted as I_p versus $\nu^{1/2}$ (Figures S14–S19). Linear plots were obtained for all systems, and the linear regression equations were provided together with the Supporting Information (Figures S14–S19). From these linear plots, it is clear that the overall kinetics of the electrochemical reactions in the $[Fe(CN)_6]^{3-/4-}$ system follows a diffusion-controlled process. Using the Randles–Sevcik relationship, the electrochemical surface area was estimated for each modified electrode.[44] Here, I_p is the peak current; n is the number of electrons transferred; ν is the sweep rate (mV/s); D is the diffusion coefficient parameter of the $[Fe(CN)_6]^{3-/4-}$ system (7.6×10^{-6} cm^2 s^{-1}); A is the active surface area of the working electrode (cm^2); and C is the concentration of the $[Fe(CN)_6]^{3-/4-}$ probe (5×10^{-6} mol cm^{-3}).

https://doi.org/10.1021/acsami.4c02022
ACS Appl. Mater. Interfaces 2024, 16, 29374–29389

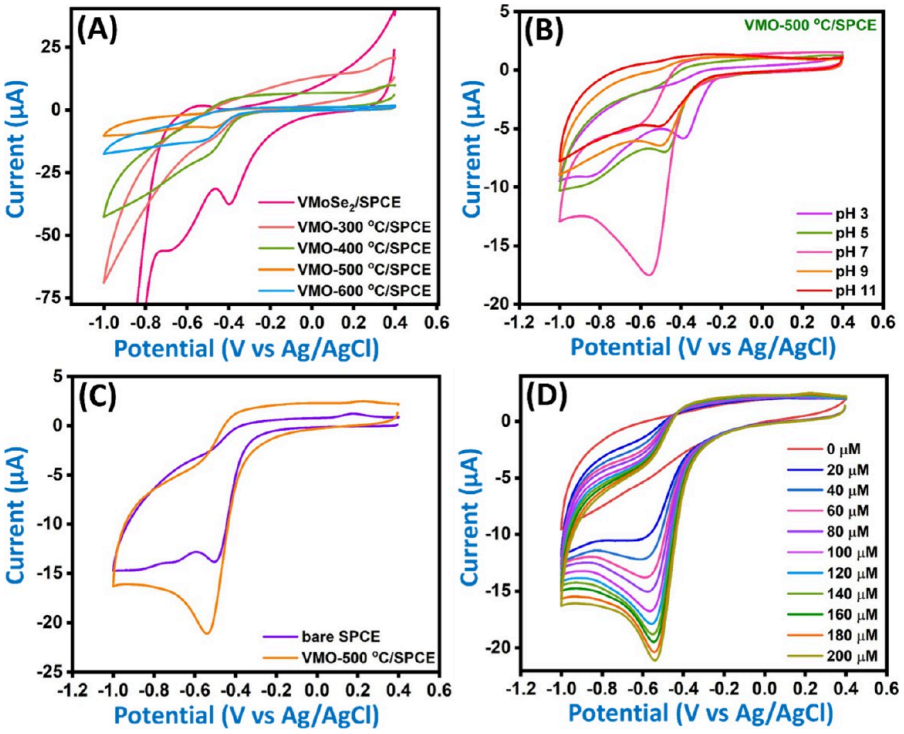

Figure 4. (A) CV response for $VMoSe_2$ and different calcined sample-modified SPCEs in the presence of 0.05 PB (pH 5) and 100 μM NFT. (B) CV response for VMO-500 °C/SPCE at different pH values (100 μM NFT). (C) CV comparison curve for bare SPCE and VMO-500 °C/SPCE in 0.05 M PB (pH 7) and 200 μM NFT. (D) CV response for different NFT concentrations (20 to 200 μM) to VMO-500 °C/SPCE.

$$I_p = (2.69 \times 10^5) n^{3/2} \nu^{1/2} D^{1/2} AC \quad (5)$$

Based on the I_p vs $\nu^{1/2}$ plots (Figures S14–S19), the electrochemical surface area was estimated for the modified electrodes $VMoSe_2$/SPCE (0.084 cm^2), VMO-300 °C/SPCE (0.053 cm^2), VMO-400 °C/SPCE (0.047 cm^2), VMO-500 °C/SPCE (0.054 cm^2), and VMO-600 °C/SPCE (0.051 cm^2). From these estimates, $VMoSe_2$ has the highest electrochemical surface area value, while the calcined samples converted to oxygen-rich VMO have electrochemical surface area values in the range of 0.047–0.054 cm^2.

3.3. Optimization Condition for NFT Detection. To investigate the electrochemical properties and sensing behavior of 2D-$VMoSe_2$ and its conversion to 1D-VMO for the detection of NFT, CV data were recorded at different pH values and scan rates. First, the modified electrodes were compared in the presence of N_2-saturated 0.05 M PB (pH 5) with 100 μM NFT by cycling between 0.4 and −1.0 V at a scan rate of 50 mV/s. The corresponding CV curves for all fabricated electrodes, including $VMoSe_2$/SPCE, VMO-300 °C/SPCE, VMO-400 °C/SPCE, VMO-500 °C/SPCE, and VMO-600 °C/SPCE, are shown in Figure 4(A). In this slightly acidic medium (pH 5), the main reduction peak for the SPCE modified with $VMoSe_2$ was observed at a potential of −0.39 V for the detection of NFT, which can be attributed to the direct conversion of the nitro (NO_2) to thehydroxylamine (−NHOH) group. The reduction current (I_{pc} = −37.53 μA) is higher than the other electrodes, which could be due to the presence of large catalytic sites on the basal plane. To confirm this phenomenon, we performed the CV test (Figure S20(A)) for different concentrations of NFT (20–100 μM) for $VMoSe_2$/SPCE under the same operating conditions. The main reduction peak at −0.39 V starts to decrease, and another redox peak at about −0.4 to 0.8 V occurs due to the redox reaction of vanadium in the acidic medium in the V–Mo structure. Figure S21 shows the complete CV curves of $VMoSe_2$/SPCE in the presence of 100 μM NFT at pH 5, indicating that the H_2 evolution reaction starts at −0.75 V.

On comparing the SPCE with the calcinated modifiers, it is evident that the VMO-300 °C/SPCE and VMO-400 °C/SPCE (Figure 4(A)) show slight evidence for the HER. This is consistent with the mixed phase of selenide and V–Mo-based oxides. On increasing the calcination temperature, the HER is inhibited, and this is clearly seen for the VMO-500 °C/SPCE and VMO-600 °C/SPCE (Figure 4(A)). The CV analysis was performed for different concentrations of NFT (20–100 μM) for all electrodes (VMO-300 °C/SPCE, VMO-400 °C/SPCE, VMO-500 °C/SPCE, and VMO-600 °C/SPCE) under the same operating conditions (0.05 PB; pH 5; 50 mV/s), and the corresponding CV curves are shown in Figure S20(B–E). While the reduction of NFT can be seen at all five electrodes, there is only a very small increase in the peak current on increasing the concentration of NFT for the $VMoSe_2$/SPCE, VMO-300 °C/SPCE, and VMO-400 °C/SPCE. This may be related to the instability of the mixed phases of V–Mo selenide and oxide or the accumulation of NFT on the electrode surface, which limits the sensing response. At the same time, optimal signal-to-noise ratio and good response to concentration variations of NFT were observed for both modified $VMoSe_2$ electrodes calcined at 500 and 600 °C. Compared to VMO-500 °C/SPCE, the VMO-600 °C/SPCE shows a slight shift in the reduction potential to higher values, which makes it less suitable for further studies. Based on these results, the calcined sample VMO-500 °C modified SPCE was used for all further studies. Interestingly, the surface area computed for the VMO-500 °C using the anionic $[Fe(CN)_6]^{3-/4-}$ electrochemical probe is much lower than that of the $VMoSe_2$.

https://doi.org/10.1021/acsami.4c02022
ACS Appl. Mater. Interfaces 2024, 16, 29374–29389

Scheme 3. Overall Electrochemical Reduction Mechanism of NFT on the Bare SPCE and Modified with VMO-500 °C

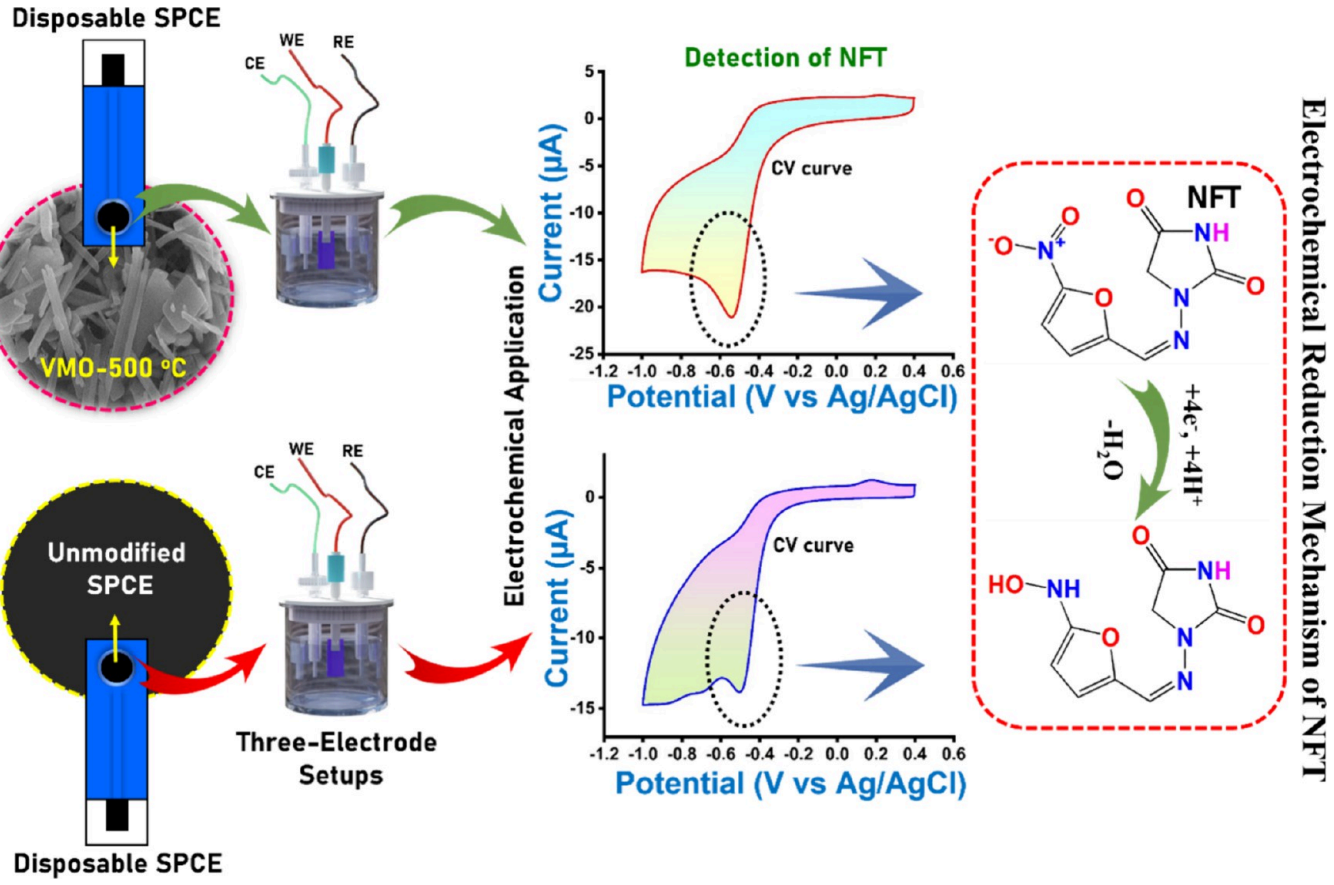

However, the VMO-500 °C is clearly more efficient in the reduction of NFT, and this seems to stem from the nature of the two analytes, with the negatively charged $[Fe(CN)_6]^{3-/4-}$ probe and the overall neutral NFT giving very different effects. Furthermore, the $VMoSe_2$ suffers from the competing hydrogen evolution reaction.

Furthermore, we investigated the electrochemical characteristics of $VMoSe_2$ and its calcined derivatives, including VMO-300 °C/SPCE, VMO-400 °C/SPCE, VMO-500 °C/SPCE, and VMO-600 °C/SPCE, in the presence of N_2-saturated 0.05 M PB (pH 7) containing 200 μM NFT. Cycling was conducted between 0.4 and −1.0 V at a scan rate of 50 mV/s. Figure S22 illustrates the corresponding CV curves for all fabricated electrodes, encompassing $VMoSe_2$/SPCE and its calcined variants. Notably, in neutral media (pH 7), the conversion of the nitro (NO_2) to the hydroxylamine (−NHOH) group exhibited enhanced peak currents and distinct reduction wave shapes compared to pH 5. $VMoSe_2$/SPCE displayed a broad reduction peak current at −0.48 V, contrasting with the other calcined samples. Interestingly, all calcined samples exhibited sharp, augmented reduction peak currents for NFT detection, each with unique peak potentials. VMO-500 °C/SPCE demonstrated enhanced peak current and nearly identical peak potential (−0.51 V) compared to VMO-300 °C/SPCE and VMO-600 °C/SPCE. Conversely, VMO-400 °C/SPCE exhibited higher peak current at slightly more negative potentials, while VMO-500 °C/SPCE demonstrated marginally lower peak potentials. As a result, VMO-500 °C/SPCE was chosen for further electrochemical investigations.

Next, the electrochemical sensing response of VMO-500 °C/SPCE for NFT in different pH media was studied. The CV experiments were performed in the presence of varying pH values (3, 5, 7, 9, and 11) containing 100 μM NFT at a scan rate of 50 mV/s. Figure 4(B) shows the CV curves obtained for different pH values. At pH values of 3 to 5 (acidic media), the reduction of NFT occurs at a lower negative potential, and the cathodic current response is low. However, the reduction of NFT in a neutral medium (pH 7) shows an excellent response with a high reduction current (−17.45 μA) at −0.55 V. When the pH is varied from 7 to 11, the cathodic current response decreases again. Moreover, we confirmed this pH variation in the cathodic peak response for the NFT sensor by performing a test with different concentrations (20−100 μM NFT) for VMO-500 °C/SPCE at all pH values (3, 5, 7, 9, and 11); the corresponding results are shown in Figure S23(A−E). These CV curves show that the cathodic peak response for NFT at different pH values (3, 5, 9, and 11) is very dependent on the pH of the solution. Low cathodic peak currents and a shift in the peak potentials to lower values are seen for the acidic and alkaline solutions, indicating poor sensing in both the acidic and basic media. At the same time, the variation of NFT concentration maintains a very good response at pH 7 (Figure S23(C)). Based on these findings, a neutral solution at a pH of 7 was chosen for all the electroanalysis studies with NFT.

3.4. Cyclic Voltammetric Comparison of NFT on Bare SPCE and VMO-500 °C/SPCE. A direct comparison of the bare SPCE and the VMO-500 °C/SPCE in 0.05 M PB saturated with N_2 (pH 7) and 200 μM NFT at a sweep rate of

https://doi.org/10.1021/acsami.4c02022
ACS Appl. Mater. Interfaces 2024, 16, 29374−29389

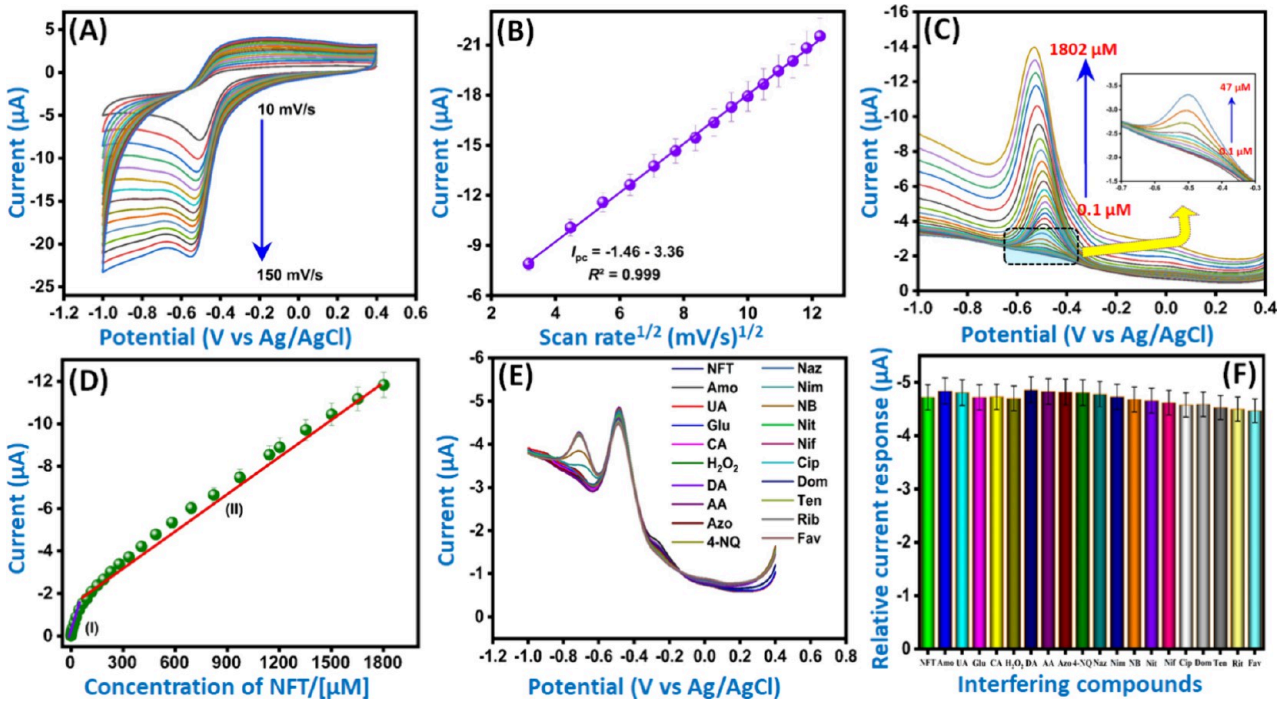

Figure 5. (A) CV responses of NFT to VMO-500 °C/SPCE at different scan rates (10−150 mV/s). (B) Linear plot for reduction peak current vs square root of scan rates. (C) DPV curves for linear addition of NFT to VMO-500 °C/SPCE in N_2 saturated in 0.05 M PB (pH 7). (D) Linear plot of reduction current vs NFT concentration, (E) anti-interference studies, and (F) corresponding bar diagram.

50 mV/s is shown in Figure 4(C). The CV curve for the bare SPCE shows the cathodic reduction peak for NFT at a potential of −0.49 V along with a reduction current response of −15.01 μA, which is comparatively lower than the surface-coated electrode (VMO-500 °C/SPCE). The lower cathodic current for NFT at the bare SPCE indicates that the carbon electrode is not able to effectively reduce the nitro compound with high sensitivity. After surface modification with VMO, a strong reduction of NFT occurs at a potential of −0.55 V, with an impressive cathodic peak current response of −21.06 μA, which is much higher than that of the bare electrode. While the cathodic peak potential is higher and less thermodynamically viable, the reduction peak current is significantly higher in the presence of the VMO. This enhanced detection of NFT may be connected to an increase in the surface-active sites due to the availability of a high density of VMO rods. In addition, the VMO possesses oxygen-rich sites with multivalent V and Mo elements that have the potential to promote the electron transfer reaction and give higher cathodic currents during electrochemical detection. These combined effects facilitate the rate of the electron transfer step and provide an excellent platform for the detection of NFT. Clearly, the crystalline 1D-VMO rods have good electrochemical sensing properties for the detection of NFT thanks to the structural transformation observed during calcination. This provides a simple strategy to give high-performing 1D materials. The electrochemical mechanism for the reduction of NFT at VMO-500 °C/SPCE and bare SPCE is shown in Scheme 3. The reduction peak at a potential of −0.55 V is related to the reduction of NFT, which involves the transfer of an equal number of electrons and protons at the surface of the electrode. No oxidation peak was observed during the reverse scan corresponding to the reduction peak, which proves that the electrochemical detection of NFT at the VMO disposable electrode is irreversible.[25]

3.5. Influence of Concentration and Scan Rate Variance on the NFT for VMO-500 °C/SPCE. To evaluate the sensing ability of the VMO-based disposable electrode, the influence of different concentrations of NFT on VMO-500 °C/SPCE was tested using the CV method. The CV test was performed under the same operating conditions (N_2 saturated 0.05 M PB: pH 7; 50 mV/s) and with the addition of different NFT concentrations from 20 to 200 μM. Figure 4(D) shows that the reduction peak current gradually increases with increasing NFT concentrations. A linear response is observed represented by a linear plot between the NFT concentration and the cathodic peak current, as shown in Figure S24, which gave a linear equation I_{pc} = −0.058 [NFT/μM] − 10.17 with a slope and regression coefficient of 0.058 μA/μM and R^2 = 0.976, respectively. In addition to measuring concentration variations, the electro-kinetic mechanism of NFT on a VMO-500 °C-based disposable electrode was investigated using the sweep rate test. The effect of lower to higher sweep rates on the cathodic response current of VMO-500 °C/SPCE for 100 μM NFT under the same working conditions was investigated using CV by applying a sweep from 10 to 150 mV/s. The cathodic current increases with increasing sweep rates (Figure 5(A)), which can be attributed to the faster diffusion of NFT due to the shorter transport path of the 1D-VMO rods at the higher scan rates. In addition, no shift in the peak potential was observed, indicating no additional diffusion layers that cause a potential shift at the higher scan rates. The effect of the sweep rate was further evaluated by plotting the cathodic peak current against the square root of the scan rate (Figure 5(B)). From this plot, a linear equation was obtained (I_{pc} (μA) = −1.46 [mV/s]$^{1/2}$ − 3.36, R^2 = 0.999), indicating that the reduction of NFT in the neutral medium is under diffusion control. To

https://doi.org/10.1021/acsami.4c02022
ACS Appl. Mater. Interfaces 2024, 16, 29374−29389

confirm that the electrode process was controlled by diffusion, the linear relationship between the logarithm of the scan rates (log v) and the logarithm of the peak current (log I_{pc}) was plotted and shown in Figure S25. In general, the slope of this linear curve is an indicator of the nature of the process: a slope close to 0.5 indicates a diffusion-controlled reaction, and a slope close to 1 indicates an adsorption-controlled reaction.[57] The linear plot shows that the value of the slope is 0.4, which is close to 0.5 and indicates that the reaction process is controlled by diffusion. Details on the kinetics of the reduction of NFT were evaluated by constructing a linear plot between E_{pc} and ln v (mV/s), which is shown in Figure S26. Using the slope of the linear plot (E_{pc} = −0.013 − 0.57, R^2 = 0.995), the general kinetic parameters, including the charge transfer coefficient (α) and the heterogeneous rate constant (K_s) for the irreversible reaction, were estimated by applying Laviron theory.[45] The K_s was computed as 0.108 $cm^2\ s^{-1}$, while α was estimated as 0.99. This indicates a reasonably high rate of electron transfer for this irreversible reaction.

3.6. Electrochemical Quantification of NFT by Differential Pulse Voltammetry (DPV) Techniques. To evaluate the electroanalytical performance, studies on the sensitivity, detection limit, and linear range of the VMO-500 °C/SPCE for the detection of NFT and DPV analysis were performed. The DPV experiment was performed at various NFT concentrations ranging from 0.1 to 1802 μM in the presence of N_2-saturated 0.05 M PB. The typical DPV curves of NFT at different concentrations are shown in Figure 5(C). Figure 5(C, inset) shows the reduction current response for the lower concentration of NFT. The DPV curves show a progressive increase in the reduction peak current with an increase in the concentration of NFT from 0.1 to 1802 μM. There is a slight shift in the position of the peak potential to more negative potentials with increasing concentrations of NFT, possibly due to the formation of additional layers of NFT molecules at the surface of the sensor. On plotting the peak current as a function of the concentration of NFT, two linear response ranges were identified. The linear plots between the cathodic peak current, I_{pc} (μA), and the concentrations of NFT (μM) (Figure 5(D)) give the corresponding linear regression equations of I_{pc} (I) = −0.028C − 0.07 for the lower concentrations and I_{pc} (II) = −0.006C − 1.54 for the higher concentrations together with correlation coefficients of (I) R^2 = 0.985 and (II) R^2 = 0.993. The detection limit (LOD) was calculated to be 0.015 μM using the equation (LOD = (3S/N)), where S is the standard deviation from the blank determination and N is the slope of the linear line. The sensitivity was computed as 0.4 $\mu A\ \mu M^{-1}\ cm^{-2}$ using the slope of (I). On comparing these analytical parameters with other previously published articles, which are summarized in Table S4, it is seen that the proposed 1D rods of VMO have a very low LOD and a wide linear response range. In particular, the work with N-CQD@Co_3O_4/MWCNT (0.04 μM),[46] the rGO/Fe_3O_4 composite (0.014 μM),[47] and functionalized carbon nanofiber/carbon black composite (0.016 μM)[48] shows comparative and higher values for LOD. Likewise, a previous report from our group, 3D flower-like neodymium molybdate (0.016 μM),[25] also showed higher LOD values for NFT determination compared to the newly proposed V−Mo-based oxide. Based on the previous literature, it is clear that the proposed VMO-modified electrodes showed comparable and improved electrochemical performance in terms of LOD and linear response range over the NFT sensor. Therefore, it is important to highlight that the disposable VMO-based electrodes presented in this work have not been described before, and their synthesis procedure is simple, fast, and inexpensive. Therefore, the main advantages of this work are the simplicity and the possibility of constructing low-cost VMO as a disposable and portable electrochemical sensing device for monitoring drug waste.

3.7. Interference Analysis of Different Species in NFT Determination. Evaluation of some common pharmaceutical excipients and their interferences is essential for the selective determination of NFT, especially in real-time monitoring of water and biological samples. Therefore, various nitro group-containing drugs/pollutants such as amoxicillin (Amo), azomycin (Azo), 4-nitroquinoline (4-NQ), nitazoxanide (Naz), nimesulide (Nim), nitrobenzene (NB), nitrendipine (Nit), nifedipine (Nif), ciprofloxacin (Cip), domperidone (Dom), tenofovir (Ten), ritonavir (Rit), and favipiravir (Fav), as well as some biomolecules such as uric acid (UA), dopamine (DA), ascorbic acid (AA), glucose (Glu), caffeic acid (CA), and hydrogen peroxide (H_2O_2), were all used for selectivity studies in the presence of NFT. With these interfering substances, the DPV experiment was performed in the presence of N_2-saturated 0.05 M PB (pH 7) containing 50 μM NFT. The above interfering substances were added at concentrations twice that of NFT, and the corresponding responses are shown in Figure 5(E). Figure 5(F) shows the bar graph of the interfering compounds and their relative current responses. In the presence of all these potential interfering substances, no significant effect is seen on the peak current of NFT at −0.49 V. Only a slight decrease in the peak current is seen in the presence of the (2-times higher) biological and nitro group drugs/pollutants. In some cases, a new cathodic peak is observed next to the NFT signal at a potential of about −0.6 to −0.8 V, which is associated with the other nitro group containing drugs/pollutants. However, these new peak signals do not affect the original current response associated with the NFT molecule. These results show that the VMO-500 °C/SPCE has excellent specificity for the detection of NFT even in the presence of some nitro group-based drugs and biomolecules.

3.8. Long-Term Stability and Real Sample Analysis of VMO-500 °C/SPCE. After testing the anti-inference nature of the proposed VMO-500 °C disposable electrode, the main factors, such as stability and real samples, were tested using the CV and DPV methods. To test the long-term storage stability of the VMO-500 °C/SPCE, the electrode was placed in N_2-saturated 0.05 M PB (pH 7) in the presence of 100 μM NFT, and CV curves were recorded at a sweep rate of 50 mV/s. The experiment was performed over a period of several days. The result shows that the proposed disposable sensor retains a signal of 95.3% of its original reduction current after 15 days of storage in a sealed container. This result indicates that the VMO-500 °C/SPCE has high durability under long-term storage. To verify the practical use of the VMO-500 °C/SPCE for the analysis of real samples, environmental samples (e.g., river, lake, and rainwater samples) and biological samples (e.g., human urine) were used. These real samples, such as rain, lake, and river water samples, were collected near Yeungnam University in South Korea. Before analysis, the collected water samples were centrifuged and cleaned of unwanted residues. The human urine samples were taken directly from a healthy male person and stored in a refrigerator to avoid contamination. However, as the real samples did not contain

https://doi.org/10.1021/acsami.4c02022
ACS Appl. Mater. Interfaces 2024, 16, 29374−29389

NFT, a known concentration was injected (see Section S2.4 for details on the preparation procedure of the real samples). The DPV method was used for the analysis, which was performed with a three-electrode system. The reduction peak signals were measured by the standard addition method by adding real samples with a known concentration of NFT (spiked samples) to 0.05 M PB. The DPV curves showing the responses for the assays are shown in Figure S27(A–E), and the results are listed in Table S5. The recoveries of NFT with VMO-500 °C/SPCE were 83.33–84.56% for lake water, 82.56–98.76% for rainwater, 83.48–90.16% for river water, and 82.11–89.9% for human urine samples. The recovery results of the developed 1D-VMO sensor are acceptable, making this sensor suitable for real-time monitoring with reasonable accuracy.

3.9. Quantum Chemical Calculations. DFT calculations were applied to investigate the mechanism by which 1D-VMO detects NFT by electrochemical reduction (EC). The calculations were performed for the possible active sites on NFT during the EC process. Figure 6(a, b) shows the optimized structure of the NFT and its LUMO surface diagram. The LUMO (E_{LUMO} = electron affinity (EA)) of an organic molecule is commonly used to describe the probable site of reduction. As shown in Figure 6(b), the LUMO regions of NFT are mainly located on the furan-NO_2 side, which would be easily hydrogenated during the reduction process of the electrode surface. Figure 6(c) shows the ESP (electrostatic potential surface) mapping of NFT, showing the location of the partially negative ESP region at O=N–O– (Mulliken atomic charge: N (0.648892), O (0.098516), O (0.046958)). The electrode surface preferentially absorbs NFT regions with negative ESP to enable a further NFT reduction process.

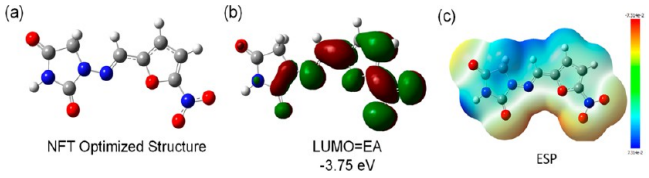

Figure 6. (a) Ground state optimized structure of NFT, (b) LUMO (= electron affinity) of NFT, and (c) electrostatic potential surface diagram of NFT.

The reduction potential of NFT was determined by the Born–Haber thermodynamic cycle (Scheme 2), which links the process in the gas phase to the solvent. The structure of the neutral and reduced forms was fully optimized. The adiabatic energies were calculated and then adjusted for thermal contributions and solvent effects to derive the Gibbs free energies for both the neutral and reduced forms; the correction is essential to meet the requirements of the Nernst equation (eq 6).

$$E^0 = \frac{-\Delta G^\circ_{solv}}{nF} \quad (6)$$

where E^0 is the reduction potential; ΔG_{solv}° is the Gibbs free energy difference between the neutral and the reduced forms in the solvent; n is the number of electrons assigned to the reaction; and F is Faraday's constant. The result shows that the reduction potential of NFT is −0.45 V. The theoretical reduction potential agrees closely with the experimental value.

4. CONCLUSIONS

The proposed work describes a simple approach, using hydrothermal synthesis followed by a temperature-controlled calcination process to prepare defect-free 1D–V-Mo-based crystalline oxides (VMO) using transition metal chalcogenide (2D-$VMoSe_2$) NSs as the primary source. Various analytical and spectroscopic techniques confirmed the formation of mixed-phase oxides/1D-VMO and $VMoSe_2$ materials. After confirming the formation of the VMO phase, the rods were subjected to electrochemical characterization to evaluate their electrochemical behavior and sensing capability using various techniques such as CV and DPV analysis. The proposed 1D-VMO rod modified SPCEs showed a low detection limit, wider linear response ranges, and good sensitivity for the detection of NFT in a neutral medium. Moreover, the VMO-500 °C/SPCE showed excellent selectivity even in the presence of other nitro group-based drugs/pollutants. In particular, the developed VMO-500 °C disposable electrode provided acceptable recovery results for NFT using the standard addition method in the analysis of real samples such as human urine, river, lake, and rainwater samples. The work concludes that the preparation of binary metal oxides derived from layered 2D metal selenides represents a new and straightforward approach for the fabrication of oxide-based electrochemical sensors aimed at the on-site detection of various drug pollutants in environmental systems.

■ ASSOCIATED CONTENT

Supporting Information

The Supporting Information is available free of charge at https://pubs.acs.org/doi/10.1021/acsami.4c02022.

Chemicals and reagents; Characterization techniques; Fabrication of electrodes and electrochemical measurements; Real sample preparation; DLS analysis for 1D-VMO-500 °C; X-ray diffraction pattern of VMO-500 °C with the standard patterns; Typical Rietveld refinement plot (VMO-500 °C); Structural parameters from the Rietveld refinement (Table S1); Lattice parameters from the obtained XRD data (Table S2); Thermogravimetric analysis (TGA) of as-prepared $VMoSe_2$; Photocopies before and after calcination of $VMoSe_2$; EDAX results for $VMoSe_2$ NSs and VMO-500 °C rods; FE-SEM image and elemental mapping results of $VMoSe_2$ NSs, VMO-300 °C, VMO-400 °C, and VMO-600 °C; DLS analysis of $VMoSe_2$-500 °C; FE-TEM image of 2D layered $VMoSe_2$; Line profile for interlayer spacing from IFFT pattern (VMO-500 °C); EIS spectra and CV curves in a 0.005 M $[Fe(CN)_6]^{3-/4-}$/0.1 M KCl redox probe for bare SPCE, $VMoSe_2$, and VMO-500 °C/SPCE; EIS data fitting values for bare SPCE, $VMoSe_2$, and VMO-500 °C (Table S3); CV response and linear plots (I_p and $\nu^{1/2}$) of bare SPCE, $VMoSe_2$, VMO-300 °C, VMO-400 °C, VMO-500 °C, and VMO-600 °C in $[Fe(CN)_6]^{3-/4-}$ redox probes at various scan rates; CV response of different concentrations of NFT (20–100 μM; 0.05 M PB; pH 5) for $VMoSe_2$ and different temperature calcined $VMoSe_2$ sample-modified SPCE; CV response of $VMoSe_2$/SPCE in the presence of 100 μM NFT (pH 5); CV response for $VMoSe_2$ and different calcined samples in 0.05 M PB (pH 7); CV response for different concentrations of NFT (20–100 μM) in various pH (3, 5, 7, 9, and 11) at calcined sample (VMO-500 °C)-

https://doi.org/10.1021/acsami.4c02022
ACS Appl. Mater. Interfaces 2024, 16, 29374–29389

modified SPCE; Linear plot for reduction peak current versus NFT concentration; Plot of log peak current vs log scan rate; Linear plot for E_{pc} versus ln v; Comparison of the NFT sensor with different modified electrodes (Table S4); Real sample analysis results using the VMO-500 °C-modified SPCE (Table S5); DPV curves for the analysis of real samples of various water samples (i.e., river, rain, and lake water) and human urine on the VMO-500 °C/SPCE; and References (PDF)

AUTHOR INFORMATION

Corresponding Authors

Ramaraj Sukanya − *Department of Chemistry, Maynooth University, Maynooth, Co. Kildare, Ireland;* orcid.org/0000-0002-9033-4201; Email: sukanya.ramaraj@mu.ie

Carmel B. Breslin − *Department of Chemistry, Maynooth University, Maynooth, Co. Kildare, Ireland;* orcid.org/0000-0002-0586-5375; Email: carmel.breslin@mu.ie

Jae-Jin Shim − *School of Chemical Engineering, Yeungnam University, Gyeongsan, Gyeongbuk 38541, The Republic of Korea;* orcid.org/0000-0002-8027-9886; Email: jjshim@yu.ac.kr

Authors

Raj Karthik − *School of Chemical Engineering, Yeungnam University, Gyeongsan, Gyeongbuk 38541, The Republic of Korea; Centre of Molecular Medicine and Diagnostics (COMManD), Department of Biochemistry, Saveetha Dental College and Hospitals, Saveetha Institute of Medical and Technical Sciences (SIMATS), Saveetha University, Chennai 600 077, India;* orcid.org/0000-0002-8605-643X

Prajakta R. Chavan − *School of Chemical Engineering, Yeungnam University, Gyeongsan, Gyeongbuk 38541, The Republic of Korea*

Mahmudul Hasan − *School of Chemical Engineering, Yeungnam University, Gyeongsan, Gyeongbuk 38541, The Republic of Korea*

Eswaran Kamaraj − *School of Chemical Engineering, Yeungnam University, Gyeongsan, Gyeongbuk 38541, The Republic of Korea*

Jintae Lee − *School of Chemical Engineering, Yeungnam University, Gyeongsan, Gyeongbuk 38541, The Republic of Korea*

Complete contact information is available at: https://pubs.acs.org/10.1021/acsami.4c02022

Notes

The authors declare no competing financial interest.

ACKNOWLEDGMENTS

This publication has emanated from research conducted with the financial support of the European Union's Horizon 2020 research and innovation programme under the Marie Skłodowska-Curie grant agreement no. 101106064. This study was supported by the National Research Foundation (NRF) of The Republic of Korea under the Consolidator Grant Program (NRF-2023R1A2C2007955), funded by the Ministry of Science and ICT, The Republic of Korea.

REFERENCES

(1) Sun, Y.; Hu, X.; Luo, W.; Shu, J.; Huang, Y. Self-assembly of hybrid $Fe_2Mo_3O_8$-reduced graphene oxide nanosheets with enhanced lithium storage properties. *J. Mater. Chem. A* **2013**, *1*, 4468.

(2) Zhu, Y.; Zhong, Y.; Chen, G.; Deng, X.; Cai, R.; Li, L.; Shao, Z. A hierarchical $Zn_2Mo_3O_8$ nanodots-porous carbon composite as a superior anode for lithium-ion batteries. *Chem. Commun.* **2016**, *52*, 9402−9405.

(3) Maseed, H.; Petnikota, S.; Srikanth, V. V. S. S.; Srinivasan, M.; Chowdari, B. V. R.; Reddy, M. V.; Adams, S. $Fe_2Mo_3O_8$/exfoliated graphene oxide: solid-state synthesis, characterization and anodic application in Li-ion batteries. *New J. Chem.* **2018**, *42*, 12817.

(4) Li, M.; Zhe, T.; Li, F.; Li, R.; Bai, F.; Jia, P.; Bu, T.; Xu, Z.; Wang, L. Hybrid structures of cobalt-molybdenum bimetallic oxide embedded in flower-like molybdenum disulfide for sensitive detection of the antibiotic drug nitrofurantoin. *J. Hazard. Mater.* **2022**, *435*, No. 129059.

(5) Zhao, D.; Qin, J.; Zheng, L.; Cao, M. Amorphous Vanadium Oxide/Molybdenum Oxide Hybrid with Three Dimensional Ordered Hierarchically Porous Structure as a High-Performance Li-Ion Battery Anode. *Chem. Mater.* **2016**, *28*, 4180−4190.

(6) Qu, G.; Wang, J.; Liu, G.; Tian, B.; Su, C.; Chen, Z.; Rueff, J. P.; Wang, Z. Vanadium Doping Enhanced Electrochemical Performance of Molybdenum Oxide in Lithium-Ion Batteries. *Adv. Funct. Mater.* **2019**, *29*, No. 1805227.

(7) Wang, J.; Tran, D. T.; Chang, K.; Prabhakaran, S.; Kim, D. H.; Kim, N. H.; Lee, J. H. Bifunctional Catalyst Derived from Sulfur-Doped $VMoO_x$ Nanolayer Shelled Co Nanosheets for Efficient Water Splitting. *ACS Appl. Mater. Interfaces* **2021**, *13*, 42944−42956.

(8) Monsef, R.; Salavati-Niasari, M. Electrochemical sensor based on a chitosan-molybdenum vanadate nanocomposite for detection of hydroxychloroquine in biological samples. *J. Colloid Interface Sci.* **2022**, *613*, 1−14.

(9) Monsef, R.; Ghiyasiyan-Arani, M.; Salavati-Niasari, M. Design of Magnetically Recyclable Ternary Fe_2O_3/$EuVO_4$/g-C_3N_4 Nanocomposites for Photocatalytic and Electrochemical Hydrogen Storage. *ACS Appl. Energy Mater.* **2021**, *4*, 680−695.

(10) Panahi, A.; Monsef, R.; Imran, M. K.; Mahdi, A. A.; Ruhaima, A. A. K.; Niasari, M. S. $TmVO_4$/Fe_2O_3 nanocomposites: Sonochemical synthesis, characterization, and investigation of photocatalytic activity. *Int. J. Hydrog. Energy* **2023**, *48*, 3916−3930.

(11) Reddy, M. A.; Kishore, M. S.; Pralong, V.; Caignaert, V.; Varadaraju, U. V.; Raveau, B. Electrochemical performance of $VoMoO_4$ as negative electrode material for Li ion batteries. *J. Power Sources.* **2007**, *168*, 509−512.

(12) Miao, X.; Chen, Z.; Wang, N.; Nuli, Y.; Wang, J.; Yang, J.; Hirano, S. Electrospun V_2MoO_8 as a cathode material for rechargeable batteries with Mg metal anode. *Nano Energy* **2017**, *34*, 26−35.

(13) Wang, X.; Pless, J. D.; Griend, D. A. V.; Stair, P. C.; Poeppelmeier, K. R.; Hu, Z.; Jorgensen, J. D. Vanadium, and molybdenum disorder in $M_{2.5}VMoO_8$ (M = Mg, Mn, and Zn) determined with neutron powder diffraction and phase formation studies of $Mg_{2.5+x}V_{1+2x}Mo_{1-2x}O_8$. *J. Alloys Compd.* **2004**, *379*, 87−94.

(14) Karthik, R.; Kumar, J. V.; Chen, S. M.; Kokulnathan, T.; Yang, H. Y.; Muthuraj, V. Design of Novel Ytterbium Molybdate Nanoflakes Anchored Carbon Nanofibers: Challenging Sustainable Catalyst for the Detection and Degradation of Assassination Weapon (Paraoxon-Ethyl). *ACS Sustainable Chem. Eng.* **2018**, *6*, 8615−8630.

(15) Chen, T. W.; Kumar, J. V.; Chen, S. M.; Mutharani, B.; Karthik, R.; Nagarajan, E. R.; Muthuraj, V. Rational construction of novel rose petals-like yttrium molybdate nanosheets: A Janus catalyst for the detection and degradation of cardioselective β-blocker agent acebutolol. *Chem. Eng. J.* **2019**, *359*, 1472−148.

(16) Vinoth Kumar, J.; Karthik, R.; Chen, S.-M.; Natarajan, K.; Karuppiah, C.; Yang, C.-C.; Muthuraj, V. 3D Flower-Like Gadolinium Molybdate Catalyst for Efficient Detection and Degradation of Organophosphate Pesticide (Fenitrothion). *ACS Appl. Mater. Interfaces* **2018**, *10*, 15652−15664.

(17) Karthik, R.; Vinoth Kumar, J.; Chen, S.-M.; Seerangan, K.; Karuppiah, C.; Chen, T.-W.; Muthuraj, V. Investigation on the Electrocatalytic Determination and Photocatalytic Degradation of Neurotoxicity Drug Clioquinol by $Sn(MoO_4)_2$ Nanoplates. *ACS Appl. Mater. Interfaces* **2017**, *9*, 26582−26592.
(18) Karthik, R.; Karikalan, N.; Chen, S.-M.; Vinoth Kumar, J.; Karuppiah, C.; Muthuraj, V. Assessment of divergent functional properties of seed-like strontium molybdate for the photocatalysis and electrocatalysis of the postharvest scald inhibitor diphenylamine. *J. Catal.* **2017**, *352*, 606−616.
(19) Tang, J. N.; Subramanian, M. A. Novel compositions and physical property comparisons for $(A, A')_{2.5}$ $VMoO_8$ lyonsites (A = Zn, A′=Mn, Ni, Cu). *J. Solid State Chem.* **2019**, *271*, 154−161.
(20) Li, Q.; Li, Y.; Zhao, J.; Zhao, S.; Zhou, J.; Chen, C.; Tao, K.; Liu, R.; Han, L. Ultrathin nanosheet-assembled hollow microplate $CoMoO_4$ array derived from metal-organic framework for supercapacitor with ultrahigh areal capacitance. *J. Power Sources* **2019**, *430*, 51−59.
(21) Xu, X.; Zhao, C.; Liu, X.; Liu, Y.; Dong, P.; Itani, C. Metal-organic framework-derived $ZnMoO_4$ nanosheet arrays for advanced asymmetric supercapacitors. *J. Mater. Sci.: Mater. Electron.* **2020**, *31*, 3631−3641.
(22) Sukanya, R.; Ramki, S.; Chen, S. M. Ultrasound supported synthesis of tantalum carbide integrated functionalized carbon composite for the voltammetric determination of the antibacterial drug nitrofurantoin in pharmaceutical samples. *Microchim Acta* **2020**, *187*, 342.
(23) Karuppaiah, B.; Ramachandran, R.; Chen, S.-M.; Wan-Ling, S.; Wan, J. Y. Hierarchical construction, and characterization of lanthanum molybdate nanospheres as an unassailable electrode material for electrocatalytic sensing of the antibiotic drug nitrofurantoin. *New J. Chem.* **2020**, *44*, 46−54.
(24) Sargın, G.; Elbek, O.; Balantekin, C.; Meteoglu, I.; Culhacı, N. Acute respiratory distress syndrome and hepatotoxicity associated with single dose nitrofurantoin use. *Case Rep. Pulmonol.* **2012**, *2012*, 1−3.
(25) Vinoth Kumar, J.; Karthik, R.; Chen, S.-M.; Chen, K.-H.; Sakthinathan, S.; Muthuraj, V.; Chiu, T.-W. Design of novel 3D flower-like neodymium molybdate: An efficient and challenging catalyst for sensing and destroying pulmonary toxicity antibiotic drug nitrofurantoin. *Chem. Eng. J.* **2018**, *346*, 11−23.
(26) Sukanya, R.; Chen, S. M. Amorphous cobalt boride nanosheets anchored surface-functionalized carbon nanofiber: A bifunctional and efficient catalyst for electrochemical sensing and oxygen evolution reaction. *J. Colloid Interface Sci.* **2020**, *580*, 318−331.
(27) Ezhil Vilian, A.T.; Hwang, S.-K.; Bhaskaran, G.; Alhammadi, M.; Kim, S.; Tiwari, J. N.; Suk Huh, Y.; Han, Y.-K. Polypyrrole-MXene supported gold nanoparticles for the trace-level detection of nitrofurantoin. *Chem. Eng. J.* **2023**, *454*, No. 139980.
(28) Balasingam, S. K.; Lee, J. S.; Jun, Y. Few-Layered $MoSe_2$ Nanosheets as an Advanced Electrode Material for Supercapacitors. *Dalton Trans.* **2015**, *44*, 15491−15498.
(29) Sakthivel, M.; Ramaraj, S.; Chen, S. M.; Chen, T. W.; Ho, K. C. Transition-Metal-Doped Molybdenum Diselenides with Defects and Abundant Active Sites for Efficient Performances of Enzymatic Biofuel Cell and Supercapacitor Applications. *ACS Appl. Mater. Interfaces* **2019**, *11*, 18483−18493.
(30) Manolikas, C. Electron Microscopic Study of Defects in V_2MoO_8. *Mater. Res. Bull.* **1976**, *11*, 1367−1374.
(31) Xue, N.; Diao, P. Molybdenum Diselenide Nanolayers Prepared on Carbon Black as an Efficient and Stable Electrocatalyst for Hydrogen Evolution Reaction. *J. Phys. Chem. C* **2017**, *121*, 26686−26697.
(32) Li, Y.; Zhang, Q.; Song, Z.; Shu, K.; Yang, Z.; Hu, H.; Lu, Y.; Tang, X.; Zhou, X. Manipulating the morphology and the electronic structures of nickel-cobalt selenides@N-doped carbon for aqueous alkaline batteries. *Colloids Surf. A: Physicochem.* **2022**, *655*, No. 130191.
(33) Ma, W.; Yao, B.; Yang, Q.; Zhang, T.; Tian, K.; Zhang, W.; Niu, J.; Yu, Y.; Chang, Z.; He, Y. Synergetic contribution of enriched selenium vacancies and out-of-plane ferroelectric polarization in AB-stacked $MoSe_2$ nanosheets as efficient piezocatalysts for TC degradation. *New J. Chem.* **2022**, *46*, 4666.
(34) Ramaraj, S.; Sakthivel, M.; Chen, S. M.; Ho, K. C. Active-Site-Rich 1T-Phase $CoMoSe_2$ Integrated Graphene Oxide Nanocomposite as an Efficient Electrocatalyst for Electrochemical Sensor and Energy Storage Applications. *Anal. Chem.* **2019**, *91*, 8358−8365.
(35) Kesari, S.; Garg, A. B.; Clemens, O.; Joseph, B.; Rao, R. Pressure-Induced Structural Behavior of Orthorhombic $Mn_3(VO_4)_2$: Raman Spectroscopic and X-ray Diffraction Investigations. *ACS Omega* **2022**, *7*, 3099−3108.
(36) Naveenraj, R.; Arun, N. S.; Ratheesh, R. Structure, and microwave dielectric properties of low-temperature sinterable $A_{2.5}VMoO_8$ (A= Mg, Zn) molybdovanadate ceramics. *Appl. Phys. A* **2020**, *126*, 53.
(37) Smit, J. P.; Kim, H. S.; Saratovsky, I.; Stark, K. B.; Fitzgerald, G.; Zajac, G. W.; Gaillard, J. F.; Poeppelmeier, K. R.; Stair, P. C. A Spectroscopic and Computational Investigation of the Vanadomolybdate Local Structure in the Lyonsite Phase $Mg_{2.5}VMoO_8$. *Inorg. Chem.* **2007**, *46*, 6556−6564.
(38) Gaur, M. A.; Schumann, M.; Raun, K. V.; Stehle, M.; Beato, P.; Jensen, A. D.; Grunwaldt, J. D.; Hoj, M. Operando XAS/XRD and Raman Spectroscopic Study of Structural Changes of the Iron Molybdate Catalyst during Selective Oxidation of Methanol. *ChemCatChem.* **2019**, *11*, 4871−4883.
(39) Kurzawa, M.; Bosacka, M.; Jakubus, P. The structure and selected properties of $Co_{2.5}VMoO_8$. *J. Mater. Sci.* **2003**, *38*, 3137−3142.
(40) Kim, D.; Kim, M.; Yi, J.; Nam, S. H.; Boo, J. H.; Park, Y. S.; Lee, J. Growth and Characterization of VO_2 Thin Film by Pulsed DC Sputtering of Optical Switching Applications. *Sci. Adv. Mater.* **2017**, *9*, 1415−1419.
(41) Sakthivel, M.; Ramaraj, S.; Chen, S. M.; Ho, K. C. Bimetallic vanadium cobalt diselenide nanosheets with additional active sites for excellent asymmetric pseudocapacitive performance: comparing the electrochemical performances with M-$CoSe_2$ (M = Zn, Mn, and Cu). *J. Mater. Chem. A* **2019**, *7*, 12565.
(42) Zhang, S.; Wang, G.; Jin, J.; Zhang, L.; Wen, Z.; Yang, J. Robust and Conductive Red $MoSe_2$ for Stable and Fast Lithium Storage. *ACS Nano* **2018**, *12*, 4010−4018.
(43) Vernickaite, E.; Lelis, M.; Tsyntsaru, N.; Pakstas, V.; Cesiulis, H. XPS studies on the Mo oxide-based coatings electrodeposited from highly saturated acetate bath. *CHEMIJA* **2020**, *31*, 203−209.
(44) Ghalta, R.; Kar, A. K.; Srivastava, R. Selective Production of Secondary Amine by the Photocatalytic Cascade Reaction Between Nitrobenzene and Benzyl Alcohol over Nanostructured Bi_2MoO_6 and Pd Nanoparticles Decorated with Bi_2MoO_6. *Chem. Asian J.* **2021**, *16*, 3790−3803.
(45) Sukanya, R.; Sakthivel, M.; Chen, S. M.; Chen, T. W. A new type of terbium diselenide nano octagon integrated oxidized carbon nanofiber: An efficient electrode material for electrochemical detection of morin in the food sample. *Sens. Actuators B Chem.* **2018**, *269*, 354−367.
(46) Muthu Sankar, G.; Devi, R. K.; Gopu, G. Nitrogen-doped carbon quantum dots embedded Co_3O_4 with multiwall carbon nanotubes: An efficient probe for the simultaneous determination of anticancer and antibiotic drugs. *Biosens. Bioelectron.* **2020**, *150*, No. 111947.
(47) He, B.; Li, J. A sensitive electrochemical sensor based on reduced graphene oxide/Fe_3O_4 nanorod composites for detection of nitrofurantoin and its metabolite. *Anal. Methods.* **2019**, *11*, 1427−35.
(48) Haidyrah, A. S.; Sundaresan, P.; Venkatesh, K.; Ramaraj, S. K.; Thirumalraj, B. Fabrication of functionalized carbon nanofibers/carbon black composite for electrochemical investigation of antibacterial drug nitrofurantoin. *Colloids Surf. A: Physicochem.* **2021**, *627*, No. 127112.

https://doi.org/10.1021/acsami.4c02022
ACS Appl. Mater. Interfaces 2024, 16, 29374−29389

(49) Wang, T.; Brudvig, G.; Batista, V. S. Characterization of proton coupled electron transfer in a biomimetic oxomanganese complex: evaluation of the DFT B3LYP level of theory. *J. Chem. Theory Comput.* **2010**, *6*, 755−760.
(50) Assary, R. S.; Brushett, F. R.; Curtiss, L. A. Reduction potential predictions of some aromatic nitrogen-containing molecules. *RSC Adv.* **2014**, *4*, 57442−57451.
(51) Saikumari, N.; Dev, S. M.; Dev, S. A. Effect of Calcination Temperature on the Properties and Applications of Bioextract-Mediated Titania Nanoparticles. *Sci. Rep.* **2021**, DOI: 10.1038/s41598-021-80997-z.
(52) Académie des Sciences (Paris). *Comptes rendus hebdomadaires des séances de l'Académie des sciences*; Gauthier-Villars, 1853; Vol. *31*.
(53) Sitepu, H. Texture and Structural Refinement Using Neutron Diffraction Data from Molybdite (MoO_3) and Calcite ($CaCO_3$) Powders and a Ni-Rich $Ni_{50.7}Ti_{49.30}$ Alloy. *Powder Diffraction* **2009**, *24*, 315−326.
(54) Oloye, F. F. Raman spectroscopy and XRD study on molybdenum oxide supported titania. *Results in Mater.* **2020**, *5*, No. 100064.
(55) Dieterle, M.; Mestl, G. Raman spectroscopy of molybdenum oxides: Part II. Resonance Raman spectroscopic characterization of the molybdenum oxides Mo_4O_{11} and MoO_2. *Phys. Chem. Chem. Phys.* **2002**, *4*, 822−826.
(56) Pacholski, C.; Kornowski, A.; Weller, H. Self-Assembly of ZnO: From Nanodots to Nanorods. *Angew. Chem., Int. Ed.* **2002**, *41*, 1188−1201.
(57) Gopu, G.; Muralidharan, B.; Vedhi, C.; Manisankar, P. Determination of three analgesics in pharmaceutical and urine sample on nano poly (3, 4-ethylenedioxythiophene) modified electrode. *Ionics* **2012**, *18*, 231−239.